Draft: June 26, 2017
Preprint typeset using LaTeX style emulateapj v. 12/16/11

THE ATACAMA COSMOLOGY TELESCOPE: TWO-SEASON ACTPOL SPECTRA AND PARAMETERS

Thibaut Louis[1,2], Emily Grace[3], Matthew Hasselfield[4,5], Marius Lungu[6], Loïc Maurin[7], Graeme E. Addison[8], Peter A. R. Ade[9], Simone Aiola[3,10,11], Rupert Allison[2], Mandana Amiri[12], Elio Angile[6], Nicholas Battaglia[13], James A. Beall[14], Francesco de Bernardis[15], J Richard Bond[16], Joe Britton[14], Erminia Calabrese[2,9], Hsiao-mei Cho[14], Steve K. Choi[3], Kevin Coughlin[17], Devin Crichton[8], Kevin Crowley[3], Rahul Datta[17], Mark J. Devlin[6], Simon R. Dicker[6], Joanna Dunkley[2,3,13], Rolando Dünner[7], Simone Ferraro[18], Anna E. Fox[14], Patricio Gallardo[15,19], Megan Gralla[20], Mark Halpern[12], Shawn Henderson[15], J. Colin Hill[21], Gene C. Hilton[14], Matt Hilton[22], Adam D. Hincks[12,23], Renée Hlozek[24], S.P. Patty Ho[3], Zhiqi Huang[16], Johannes Hubmayr[14], Kevin M. Huffenberger[25], John P. Hughes[26], Leopoldo Infante[19], Kent Irwin[27], Simon Muya Kasanda[22,28], Jeff Klein[6], Brian Koopman[15], Arthur Kosowsky[10,11], Dale Li[14], Mathew Madhavacheril[29], Tobias A. Marriage[8], Jeff McMahon[17], Felipe Menanteau[30,31], Kavilan Moodley[22], Charles Munson[17], Sigurd Naess[2], Federico Nati[6,32], Laura Newburgh[24], John Nibarger[14], Michael D. Niemack[15], Michael R. Nolta[16], Carolina Nuñez[13,19,33], Lyman A. Page[3], Christine Pappas[3], Bruce Partridge[34], Felipe Rojas[19,32], Emmanuel Schaan[13], Benjamin L. Schmitt[6], Neelima Sehgal[29], Blake D. Sherwin[18], Jon Sievers[28,35], Sara Simon[3], David N. Spergel[13,36], Suzanne T. Staggs[3], Eric R. Switzer[16,37], Robert Thornton[6,38], Hy Trac[33], Jesse Treu[3], Carole Tucker[9], Alexander Van Engelen[16], Jonathan T. Ward[6], Edward J. Wollack[37]

Draft: June 26, 2017

ABSTRACT

We present the temperature and polarization angular power spectra measured by the Atacama Cosmology Telescope Polarimeter (ACTPol). We analyze night-time data collected during 2013–14 using two detector arrays at 149 GHz, from 548 deg^2 of sky on the celestial equator. We use these spectra, and the spectra measured with the MBAC camera on ACT from 2008–10, in combination with *Planck* and *WMAP* data to estimate cosmological parameters from the temperature, polarization, and temperature-polarization cross-correlations. We find the new ACTPol data to be consistent with the ΛCDM model. The ACTPol temperature-polarization cross-spectrum now provides stronger constraints on multiple parameters than the ACTPol temperature spectrum, including the baryon density, the acoustic peak angular scale, and the derived Hubble constant. The new ACTPol data provide information on damping tail parameters. The joint uncertainty on the number of neutrino species and the primordial helium fraction is reduced by 20% when adding ACTPol to Planck temperature data alone.

[1] UPMC Univ Paris 06, UMR7095, Institut d'Astrophysique de Paris, F-75014, Paris, France
[2] Sub-Department of Astrophysics, University of Oxford, Keble Road, Oxford, UK OX1 3RH
[3] Joseph Henry Laboratories of Physics, Jadwin Hall, Princeton University, Princeton, NJ, USA 08544
[4] Department of Astronomy and Astrophysics, The Pennsylvania State University, University Park, PA 16802
[5] Institute for Gravitation and the Cosmos, The Pennsylvania State University, University Park, PA 16802
[6] Department of Physics and Astronomy, University of Pennsylvania, 209 South 33rd Street, Philadelphia, PA, USA 19104
[7] Instituto de Astrofísica and Centro de Astro-Ingeniería, Facultad de Física, Pontificia Universidad Católica de Chile, Av. Vicuña Mackenna 4860, 7820436 Macul, Santiago, Chile
[8] Dept. of Physics and Astronomy, The Johns Hopkins University, 3400 N. Charles St., Baltimore, MD, USA 21218-2686
[9] School of Physics and Astronomy, Cardiff University, The Parade, Cardiff, Wales, UK CF24 3AA
[10] Department of Physics and Astronomy, University of Pittsburgh, Pittsburgh, PA, USA 15260
[11] Pittsburgh Particle Physics, Astrophysics, and Cosmology Center, University of Pittsburgh, Pittsburgh PA 15260
[12] Department of Physics and Astronomy, University of British Columbia, Vancouver, BC, Canada V6T 1Z4
[13] Department of Astrophysical Sciences, Peyton Hall, Princeton University, Princeton, NJ USA 08544
[14] NIST Quantum Devices Group, 325 Broadway Mailcode 817.03, Boulder, CO, USA 80305
[15] Department of Physics, Cornell University, Ithaca, NY, USA 14853
[16] Canadian Institute for Theoretical Astrophysics, University of Toronto, Toronto, ON, Canada M5S 3H8
[17] Department of Physics, University of Michigan, Ann Arbor, USA 48103
[18] Berkeley Center for Cosmological Physics, LBL and Department of Physics, University of California, Berkeley, CA, USA 94720
[19] Departamento de Astronomía y Astrofísica, Pontificía Universidad Católica, Casilla 306, Santiago 22, Chile
[20] Steward Observatory, University of Arizona. 933 North Cherry Avenue, Tucson, AZ 85721
[21] Dept. of Astronomy, Pupin Hall, Columbia University, New York, NY 10027 USA
[22] Astrophysics and Cosmology Research Unit, School of Mathematics, Statistics and Computer Science, University of KwaZulu-Natal, Durban 4041, South Africa
[23] Department of Physics, University of Rome "La Sapienza", Piazzale Aldo Moro 5, I-00185 Rome, Italy.
[24] Dunlap Institute, University of Toronto, 50 St. George St., Toronto, ON, Canada M5S3H4
[25] Department of Physics, Florida State University, Tallahassee FL, USA 32306
[26] Department of Physics and Astronomy, Rutgers, The State University of New Jersey, Piscataway, NJ USA 08854-8019
[27] Department of Physics, Stanford University, Stanford, CA, USA 94305-4085
[28] Astrophysics and Cosmology Research Unit, School of Chemistry and Physics, University of KwaZulu-Natal, Durban 4041, South Africa
[29] Physics and Astronomy Department, Stony Brook University, Stony Brook, NY USA 11794
[30] National Center for Supercomputing Applications (NCSA), University of Illinois at Urbana-Champaign, 1205 W. Clark St., Urbana, IL, USA, 61801

1. INTRODUCTION

The now standard ΛCDM model of cosmology has been increasingly refined with measurements of the cosmic microwave background (CMB), most recently by the *Planck* satellite (Planck Collaboration et al. 2014a, 2016c). This model provides an excellent fit to current cosmological data but leaves unanswered questions about the contents, structure and dynamics of the Universe, and their origins. Some tensions exist at the 2-3σ significance level between the Hubble constant and the amplitude of fluctuations derived from different cosmological probes (e.g., Riess et al. 2016; Hildebrandt et al. 2016). One of the paths forward is an improved measurement of the polarization anisotropy and its power spectra.

Significant new CMB polarization data have been published in the last three years. The *Planck* team reports TE and EE polarization spectra for $\ell \geq 50$ from the HFI instrument (Planck Collaboration et al. 2016c), and estimates the large-scale E-mode signal from the LFI and HFI instruments (Planck Collaboration et al. 2016b,h). The E-mode power spectrum has also been measured by *WMAP* on large scales (Hinshaw et al. 2013), and on smaller scales with first-season ACTPol data (Naess et al. 2014), by BICEP2/Keck (BICEP2 Collaboration et al. 2016), The Polarbear Collaboration: P. A. R. Ade et al. (2014), and SPTpol (Crites et al. 2015). These all show the E-mode signal to be consistent with the ΛCDM prediction.

The B-mode gravitational lensing signal has now been measured at 2σ by the The Polarbear Collaboration: P. A. R. Ade et al. (2014), at 4σ by SPTpol (Keisler et al. 2015), and at 7σ by BICEP2/Keck (BICEP2 Collaboration et al. 2016). It has been detected in cross-correlation with the reconstructed lensing signal by SPTpol (Hanson et al. 2013), The Polarbear Collaboration: Ade et al. (2014), ACTPol (van Engelen et al. 2015), and *Planck* (Planck Collaboration et al. 2016d).

This paper describes the temperature and polarization power spectra and derived cosmological parameters obtained from two seasons of observations by the Atacama Cosmology Telescope Polarimeter (ACTPol). In this analysis we use only data collected at night in a 548 deg^2 region known as 'D56.' In §2 we describe the data and basic processing, and in §3 show the power spectra and null tests. In §4 we describe our likelihood method, in §5 show cosmological results, and conclude in §6. The lensing analysis of this data set is presented in Sherwin et al. (2016) .

[31] Department of Astronomy, University of Illinois at Urbana-Champaign, W. Green Street, Urbana, IL, USA, 61801
[32] Sociedad Radiosky Asesorías de Ingeniería Limitada Lincoyán 54, Depto 805 Concepción, Chile
[33] McWilliams Center for Cosmology, Carnegie Mellon University, Department of Physics, 5000 Forbes Ave., Pittsburgh PA, USA, 15213
[34] Department of Physics and Astronomy, Haverford College, Haverford, PA, USA 19041
[35] National Institute for Theoretical Physics (NITheP), KZN node, Durban 4001, South Africa
[36] Center for Computational Astrophysics, 162 5th Ave NY NY 10003 USA
[37] NASA/Goddard Space Flight Center, Greenbelt, MD, USA 20771
[38] Department of Physics , West Chester University of Pennsylvania, West Chester, PA, USA 19383

2. DATA AND PROCESSING

In this paper we use a combination of data collected during three months of observations in 2013 using a single detector array known as PA1, as reported in Naess et al. (2014), combined with data from a four month period in 2014 using the PA1 and PA2 detector arrays. Each detector array is coupled to 522 feedhorns, and has 1044 TES bolometers operating at 149 GHz, of which a median 400 (for PA1) and 600 (for PA2) detectors are used for this analysis. Further description of the instrument is given in Naess et al. (2014) and Thornton et al. (2016).

We refer to the first-season 2013 data as S1, and the second-season 2014 data as S2. Observations of Uranus permit the direct calibration of timestream data to estimate detector sensitivities. These measurements produce array noise equivalent temperatures (NETs) of 15.3 μK$\sqrt{\text{s}}$ and 23.0 μK$\sqrt{\text{s}}$ for PA1 in S1 and S2 respectively, and 12.9 μK$\sqrt{\text{s}}$ for PA2. The sensitivities of the detector arrays depend on the loading from the sky. These values correspond to a precipitable water vapor column density, along the line of sight, of 1.2 mm, which was the median value for S2 observations. The decreased sensitivity of PA1 in S2 is due to higher average cryogenic temperatures of the detectors. Because of data cuts, the white noise levels seen in the CMB maps are 12% higher, in temperature, than the simple prediction based on these array sensitivities and the observing time.

The passbands for both PA1 and PA2 detectors were measured in the field using a Fourier Transform Spectrometer coupled to the cold optics at the receiver windows. The effective frequency for the CMB is $\nu_{\rm CMB} = 148.9 \pm 2.4$ GHz for PA1 and $\nu_{\rm CMB} = 149.1 \pm 2.4$ GHz for PA2 (Thornton et al. 2016).

2.1. *Observations*

In 2013 ACTPol observed four deep regions covering 260 deg^2 at right ascensions 150°, 175°, 355°, and 35°, known as D1, D2, D5 and D6. In the second and third seasons, ACTPol observed two wider regions, known as D56 and BOSS-N. The D56 region used for analysis covers 548 deg^2 with coordinates $-7.2° < \text{dec} < 4°$ and $-8° < \text{RA} < 41°$, and BOSS-N covers 2000 deg^2 with coordinates $-4° < \text{dec} < 20°$ and $142° < \text{RA} < 228°$. The D5 and D6 sub-regions lie within D56. The D56 and BOSS-N regions are visible to the telescope at different times of day, and each was observed both rising and setting on each day. The observations alternated, from day to day, between two different elevations, to provide a total of four different parallactic angles in the complete data set. Data were taken from Sept. 11, 2013 to Dec. 14, 2013 (S1), and Aug. 20, 2014 to Dec. 31, 2014 (S2). An overview of the entire ACTPol survey is presented in De Bernardis et al. (2016).

In this paper we analyze just the night-time data in the D56 region, including the D5 and D6 sub-regions measured in S1. These data correspond to 45% of all two-season CMB data that pass data quality screening procedures (55% of S1 and 40% of S2), and 12% of all screened three-season data. The combined maps and weight map of the two-season data are shown in Figure 1 and a summary of the data given in Table 1. As in Naess et al. (2014) we analyze only the lowest noise regions of the maps, avoiding the edges of the maps where the noise

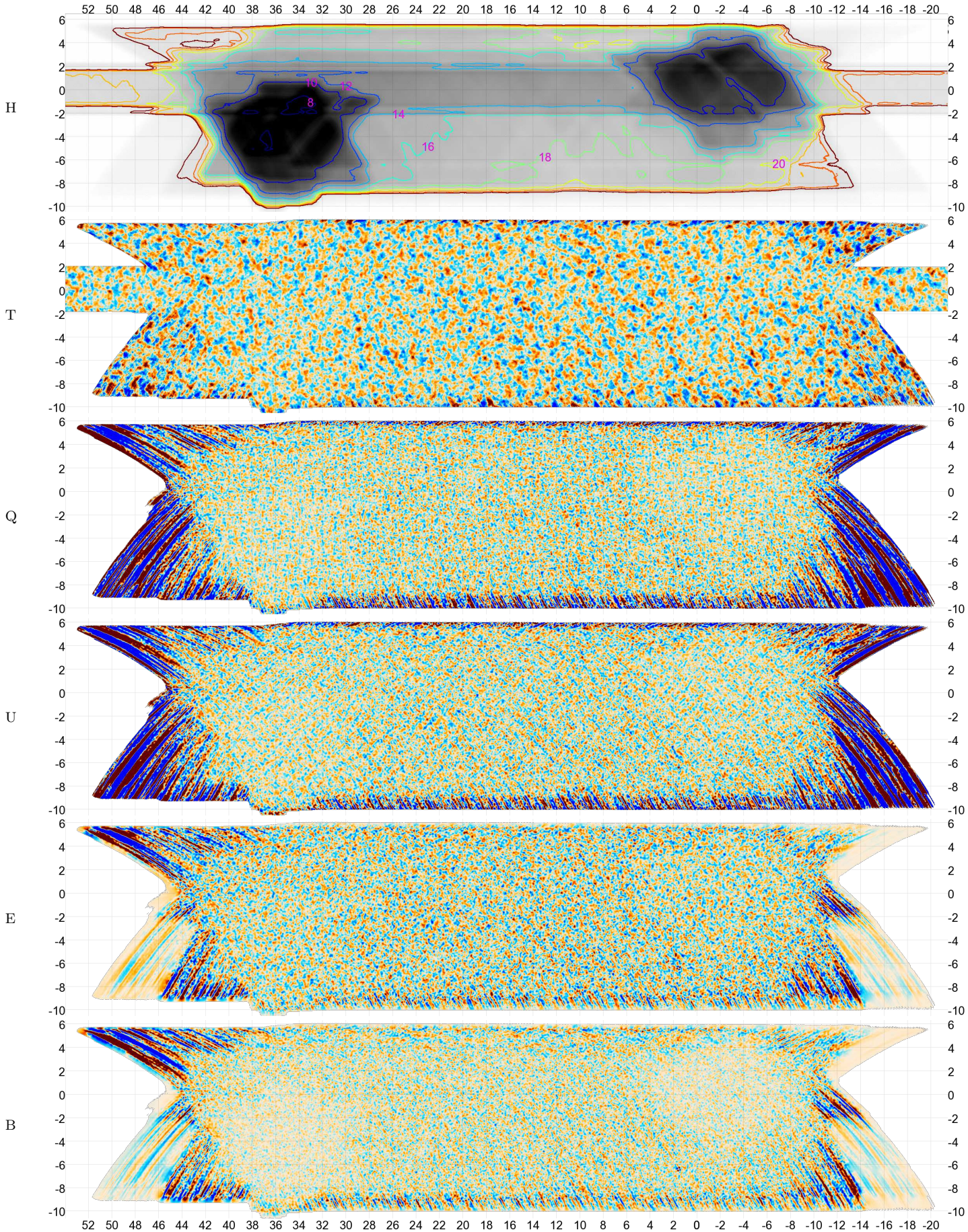

FIG. 1.— Top (H): Exposure map in equatorial coordinates (the horizontal and vertical axes are RA and Dec respectively), including both the three-season MBAC data and the ACTPol data used in this analysis. The D5 and D6 regions are the deep fields on the right and left sides of the map, and D56 is the wider rectangle which overlaps both deep fields. The contour labels indicate the T noise level in μK$\cdot$arcmin, starting from 8μK$\cdot$arcmin in the deepest region. The Q and U noise levels are each $\sqrt{2}$ higher. Lower panels: Filtered maps in T and in Q, U, E and B-polarization. All maps are filtered with a highpass-filter at $\ell = 200$ and a horizontal highpass-filter at $\ell = 40$. The polarization maps are additionally lowpass-filtered at $\ell = 1900$. The E and B maps are made using the standard flat sky decomposition of the polarization field. We apodize the map to minimize edge effects. The color scale is $\pm 250\mu$K in T and $\pm 25\mu$K in P.

TABLE 1
SUMMARY OF TWO-SEASON ACTPOL DATA USED IN THIS ANALYSIS: NIGHT-TIME DATA IN D56 REGION.

	D56	D5	D6
RA min, max(deg)	$-8.0, 41.0$	$-7.5, 2.7$	$30.0, 40.0$
Dec min, max (deg)	$-7.2, 4.0$	$-3.0, 3.8$	$-7.2, -1.0$
Analyzed area (deg^2)	548	70	63
Noise level (μK.arcmin)	17.7	12.0	10.5
Hours (S1)		222	268
Hours (S2)	709[a]		
Effective $N_{\rm det}$[b]	457	404	430

[a]Observing hours summed over the two arrays, with 337 hrs in PA1 and 372 in PA2.
[b]The total amount of data is the effective number of detectors multiplied by observing hours.

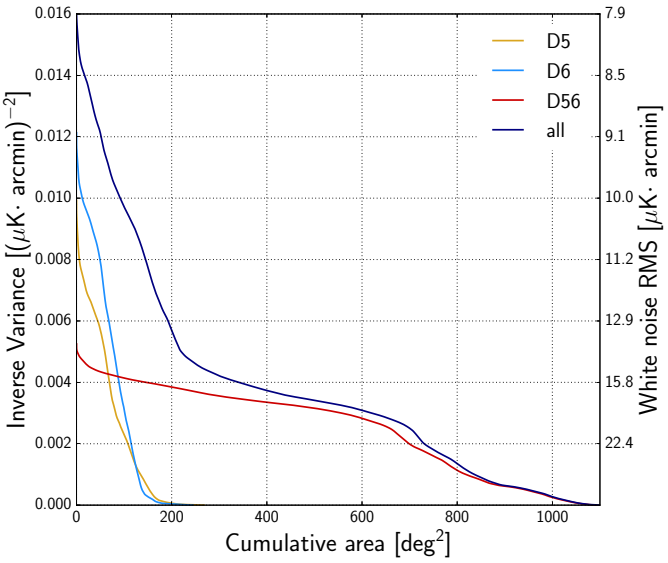

FIG. 2.— The temperature white noise levels (right axis), and inverse variance (left axis), in the ACTPol maps as a function of cumulative area. Levels are shown for the larger D56 region, the smaller D5 and D6 sub-regions, and the combined map.

properties change drastically. Combining the data from PA1 and PA2 for D56, and additionally including S1 data for D5 and D6, this results in a white noise map sensitivity of 18, 12, and 11 μK· arcmin for D56, D5 and D6 respectively, illustrated in Figure 2. To get Stokes Q or U sensitivities, multiply by $\sqrt{2}$.

2.2. *Data pre-processing*

Much of the data selection and analysis follows Naess et al. (2014) and Dünner et al. (2013); here we report changes or improvements made for this analysis.

The data selection method has been refined and sped up. The new algorithm works mainly in frequency space, assessing the data properties and systematics in different frequency bands. In the sub-Hz range, the data are dominated by atmosphere temperature brightness fluctuations, and to a lesser degree bath thermal drifts. The latter are measured and deprojected using the signal from detectors which are not optically coupled, known as dark detectors. The correlations generated by the atmospheric drifts are used to select the working detectors and measure their relative gains. The detector noise is measured at higher frequencies, between 8 and 15 Hz, after deprojecting the ten largest modes across the array corresponding to up to 10% of the total variance. Detectors with an extreme noise level, or abnormal skewness or kurtosis, which is a signature of residual contamination, are rejected from the analysis.

2.3. *Pointing and beam*

The pointing reconstruction model has been improved. The preliminary pointing model is still constrained using observations of planets at night. In this new analysis we also apply a correction to account for temporal variation in the pointing of the telescope. We first make a preliminary map with the nominal pointing estimate. We then locate bright point sources and find their true positions by matching them to known catalogs. Assuming that the beam is constant, we then take each ≈10 minute section of time-ordered data, which we term a 'TOD,' and perform a joint fit in the time domain to the four brightest sources stronger than 1 mK, fitting for a single overall pointing offset per TOD, $[p_x, p_y]$, in focal plane coordinates, and a flux for each source.

We use this primary pointing correction when a TOD has a good source fit, quantified by requiring the uncertainty on the pointing offset, $\sigma(p_{x,y})$ to be less than $12''$, which is satisfied for 65% of the data. For the remaining TODs we follow a simple prescription. If available, we use the average of nearest neighbor TODs within 15 minutes, of the same scan type with the same azimuth and elevation (24% of the data). If not available, we use secondary neighbors within 30 minutes (4.5%). If fits from neighboring TODs are not available, we use an average of offsets from the same scan type within 0.5, 1, or 1.5 hours in UTC (5%). If none of the above is possible, we use an average of all TODs with good fits within 0.5 hours in UTC (2%), which amounts to correcting for a global offset. Maps are remade with this refined pointing solution.

As in the first season, we use multiple observations of Uranus to determine the beam profile, which is modeled in one radial dimension. The beam window functions and solid angles are described in Thornton et al. (2016), and are normalized at $\ell = 1400$. The beam uncertainty is further increased due to the position-dependent pointing uncertainty. The impact of this uncertainty on the full season maps is handled by projecting the estimated pointing variance for each TOD, weighted by white noise level, into a map and finding its distribution. This is combined with an estimate made by convolving the instantaneous beam with a Gaussian, and fitting for its width using multiple bright point sources. The resuting pointing variance corrected beams, along with the instantaneous beams, are shown in Figure 3. The corrected beams are included in the covariance matrix for the power spectrum, following the same treatment as in Naess et al. (2014).

During this analysis we established the existence of weak, polarized sidelobes in the PA1 and PA2 optical systems. The sidelobes are shown in Figure 4 and consist of several slightly elongated images of the main beam, suppressed to a level below -30 dB and distributed with a rough 4-fold symmetry at a distance of approximately $15'$(with an additional set visible at $30'$in PA1). The sidelobes are strongly polarized in the direction perpendicular to the vector between the main beam and the

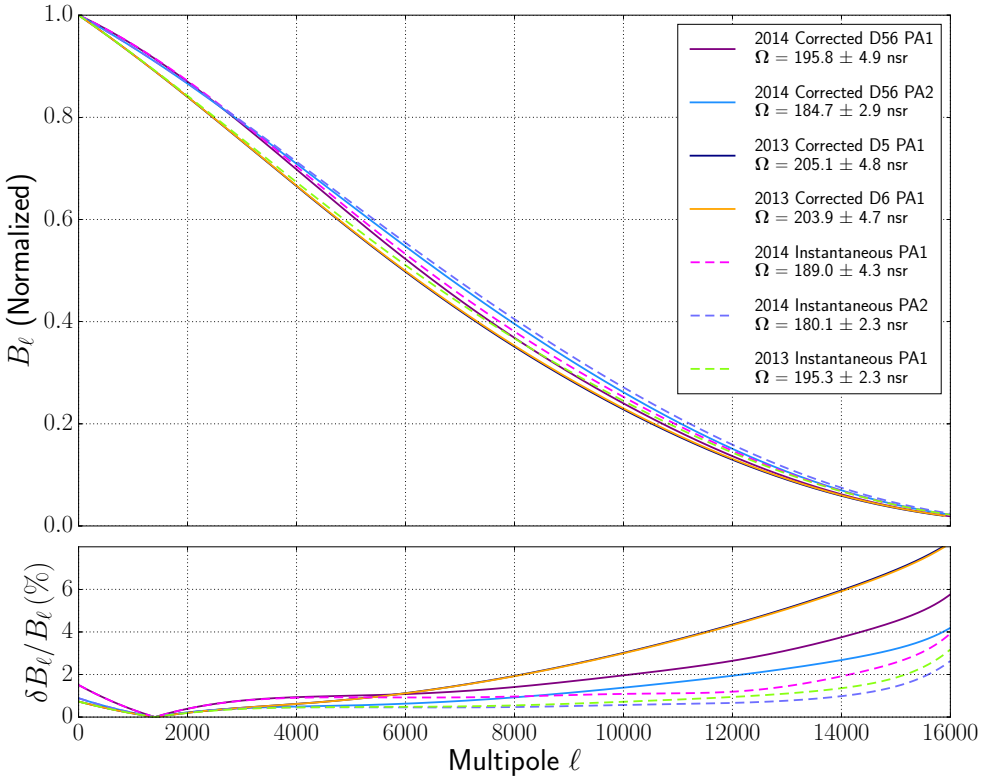

FIG. 3.— The beam window functions (top) and uncertainties (bottom) measured by ACTPol during the first (S1, 2013) and second (S2, 2014) observing seasons for the arrays PA1 and PA2. Both the instantaneous beams (dashed lines) and the pointing variance corrected beams (solid lines) for the three different regions included in the analysis are shown. The total solid angle and its uncertainty are given for each beam in units of nanosteradians (nsr).

sidelobe position, which results in a small leakage of intensity into E-mode polarization.

Studies of Saturn observations across the three ACTPol observing seasons show that the sidelobes are stable in time, and that their amplitudes are stable across the focal plane with the exception that there are no sidelobes associated with any points outside each array's field of view. The fact that sidelobes from Saturn are only seen if Saturn lies within a focal plane's field of view confirms that the effect originates inside the receiver and not in the primary or secondary optics.

To remove this effect from the maps, the sidelobe signal is projected out of the time domain data prior to the mapmaking stage. To facilitate this deprojection, the sidelobes are modeled as a combination of ≈ 20 instances of the main beam, with the T, Q, and U amplitudes (relative to the main beam in focal plane coordinates) of each instance fitted to Saturn observations. As a test of this removal process and to estimate residuals, we run Saturn observations through the map-making pipeline and demonstrate significant improvement in the TE and TB transfer functions (see Figure 4). The remaining TE and TB contamination is treated as a systematic error in the cosmological spectrum analysis. As described in the Appendix (Equation B3), the residual contamination is included with an extra term in the covariance matrix of the power spectra.

The origin of these polarized sidelobes is under investigation; the optical characteristics suggest the effect is related to the filter element near the Lyot stop. We do not observe visible sidelobes in the PA3 data, which has a different configuration of filters.

As in Naess et al. (2014), the polarization angles for the PA1 and PA2 detectors are calculated by detailed optical modeling of the mirrors, lenses and filters (Koopman et al. 2016). A rotating wire grid was used to confirm that, apart from a global offset angle, the relative orientations of the detectors differ from the optical model with an RMS of less than two degrees. Because the optical modeling ties together the positions of the detectors and their polarization angles, the measurement of the relative positions of the detectors on the sky also fixes the polarization angles of all detectors on the sky. There are thus no free parameters in mapping the optical model to the sky; work is underway to quantify any remaining systematic error in the optical modeling procedure. We later test for any additional global angle offset using the EB power spectrum.

2.4. *Mapmaking*

We continue to estimate maps using the maximum likelihood method, solving the system

$$(A^T N^{-1} A)\boldsymbol{m} = A^T N^{-1} \boldsymbol{d} \quad (1)$$

using the preconditioned conjugate gradient algorithm described in Naess et al. (2014). Here, $\boldsymbol{d}$ is the set of time-ordered data, A is the generalized pointing matrix that projects from map domain to time domain, and N is the noise covariance of the data. We make separate maps for the D56 wide region for both PA1 and PA2, and maps of the deeper D5 and D6 sub-regions for PA1. In each case we make four map-splits, allocating every fourth night of

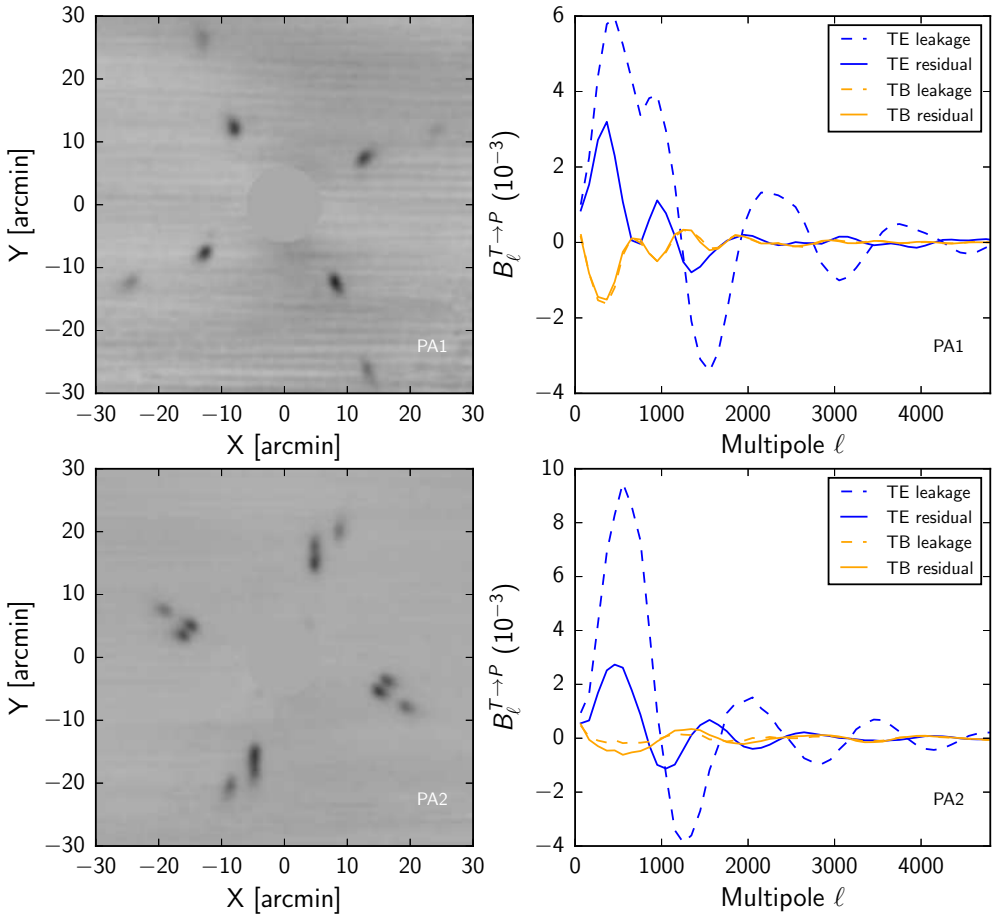

FIG. 4.— Polarized sidelobes in PA1 (top row) and PA2 (bottom row). Left panels show maps of the beam sidelobes, from 20 observations of Saturn. Spatial coordinates are relative the main beam, which is masked here. Grayscale provides the sidelobe amplitude in the range -0.002 (black) to +0.001 (white) relative to the main beam peak, with negative signal indicating polarization perpendicular to the ray from the origin. The complementary polarization component (corresponding to TB leakage) is smaller and not shown in the maps but is included in the evaluation of the transfer functions. Right panels show the TE and TB transfer functions, normalized in units of the main beam, as in Figure 3, before and after the sidelobe deprojection procedure.

data to each split. The map depths are shown in Figure 2. As in Naess et al. (2014) we use cylindrical equal area (CEA) pixels of side $0.5'$, in equatorial coordinates.

We now account for the beam sidelobes in the mapmaking as described in the previous section. We also make a set of cuts in the mapmaking step. We use the same treatment to remove scan-synchronous pick-up as in Naess et al. (2014), applying an azimuth filter to the time-ordered data. We also detect several spikes in the TOD power spectra, and mask those as a precaution. We found a few detectors occasionally deviate from the expected white-noise behavior at high frequency. To avoid giving these unrealistically high statistical weight in the mapmaking, we apply a cut requiring the noise power at 100 Hz to be no more (less) than 3 (0.5) times the power at 10 Hz.

To identify possible systematic contaminants we make maps centered on the Moon and on the Sun, as well as in coordinates fixed relative to the ground. To remove Moon contamination we make a new Moon-centered mask defined using a Sun-centered map to better measure the beam sidelobes. This new mask reduces the number of TODs by 7%, and includes masking sidelobes at 30° away from the boresight that were not masked in the original S1 maps, in addition to the two sidelobes at 20° and 120° identified in Naess et al. (2014).

To remove ground or other scan-synchronous pickup contamination we bin each detector's data by azimuth for each of the different scanning patterns. Several classes of near-constant excess signal are observed for groups of detectors at particular regions of azimuth and elevation. Some of these we attribute to ground pick-up, but most of them appear to be internal to the telescope. We mask these regions, corresponding to removing 6% of the data. These cuts will be described more fully in a follow-up paper. Their effect on the spectra is tested in one of our null tests.

Finally, we re-estimate the transfer function for these new maps, finding it to decrease from 0.995 at $\ell = 500$ to 0.95 at $\ell = 200$.

A 45 deg^2 cut-out of the ACTPol temperature map is shown in Figure 5, compared to the corresponding part of the *Planck* 143 GHz map. This region covers the transition from the deep to the shallower part of the ACTPol data. The two maps are in good agreement; a quantitative comparison of the data is presented in Section 3.

3. ANGULAR POWER SPECTRA

3.1. *Methods*

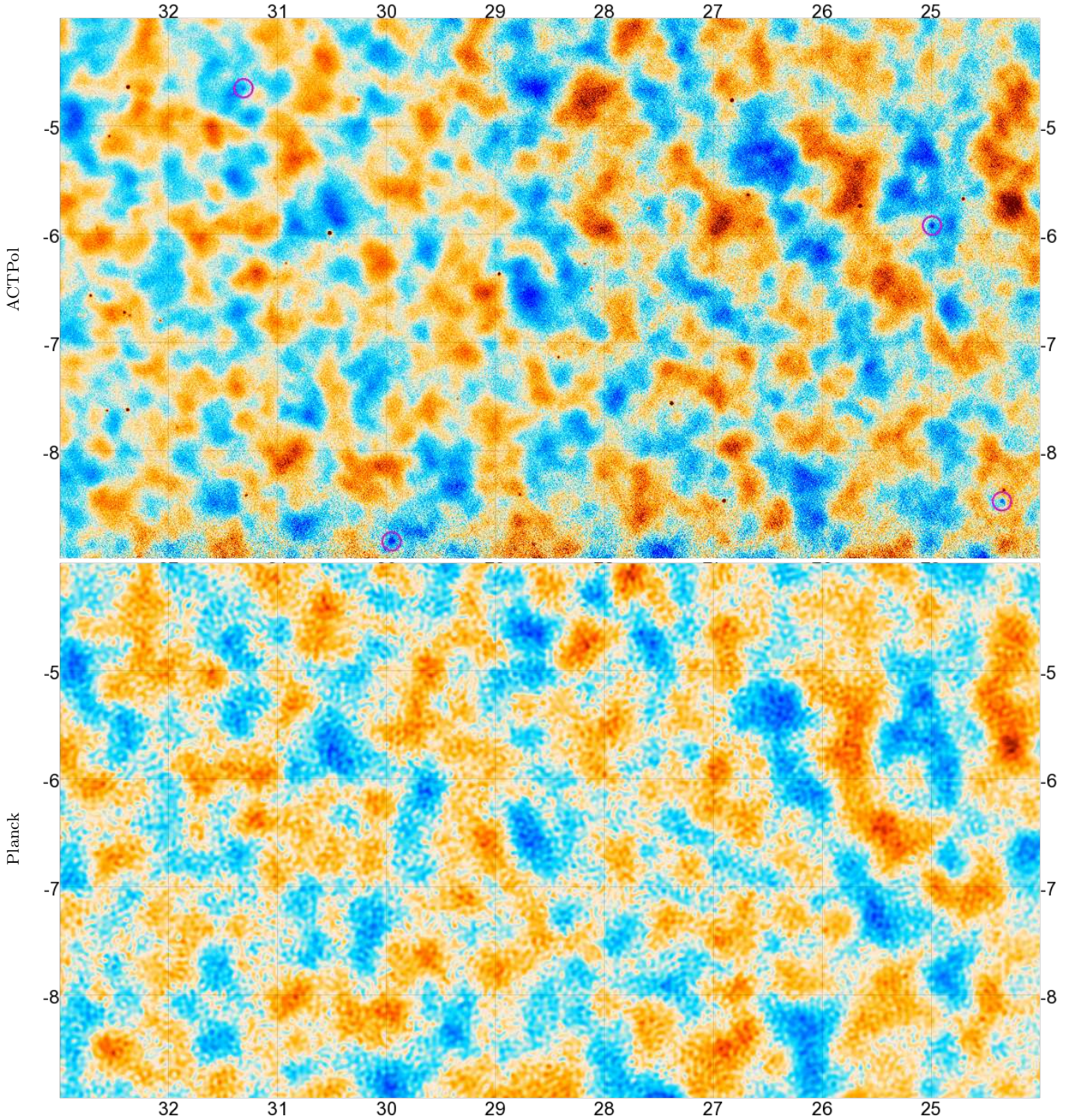

FIG. 5.— A 45 deg^2 subset of the map in full resolution in T showing ACTPol 149 GHz (top) and Planck 143 GHz (bottom), in equatorial coordinates, both filtered as in Figure 1. The color scale is $\pm 250\mu$K. This region covers the transition from deep (top left, sensitivity $10\mu\text{K} \cdot \text{arcmin}$) to shallow (right, $16\mu\text{K} \cdot \text{arcmin}$) exposure, and represents about 8% of the usable area in D56. The two maps are in good agreement. Several point sources (red dots) and SZ clusters (circled) are visible in the ACTPol map. The identified clusters are ACT-CL J0137.4-0827, ACT-CL J0140.0-0554, ACT-CL J0159.8-0849 (all previously found in other cluster surveys), and ACT-CL J0205.3-0439 (reported in Naess et al. (2014)). Their details will be given in a forthcoming paper.

We follow the methods described in Louis et al. (2013) and Naess et al. (2014) to compute the binned angular power spectra using the flat-sky approximation. This is a standard pseudo-C_ℓ approach that accounts for the masking and window function with a mode-coupling matrix. In this analysis we do not use the pure B-mode estimator as in Smith (2006) as our focus is on E-modes. We compute cross-spectra from four map-splits, and following Das et al. (2014) and Naess et al. (2014) we mask Fourier modes with $|k_x| < 90$ and $|k_y| < 50$ to remove scan-synchronous contamination. We identify bright point sources in the intensity map, and mask 273 sources with flux brighter than 15 mJy using a circle of radius $5'$. We do not mask any polarized point sources or SZ clusters, but we identify one bright polarized point source at a previously-known source location RA = 1.558°, Dec = -6.396°. We present power spectra in the range $500 < \ell < 9000$ in temperature and $350 < \ell < 9000$ in polarization, chosen to minimize atmospheric contamination, large-scale systematic contamination, and to avoid angular scales where the transfer function deviates from unity by more than a percent.

We compute the power spectra for D56 (PA1×PA1, PA2×PA2, and PA1×PA2), for D5 and D6 PA1×PA1, and for the cross-correlation between the deep regions (D5, D6) and D56. As in Naess et al. (2014) we use the notation $\mathcal{D}_\ell^{\rm XY} = \ell(\ell+1)C_\ell^{\rm XY}/2\pi$ where XY ∈ TT, TE, TB, EE, EB, BB. The covariance matrix for these spectra is estimated using simulations described below, and are compared to an analytic estimate in the Appendix. We then optimally combine the spectra to produce a single 149 GHz power spectrum for each combination XY. The method for doing this coaddition is also described in the Appendix. The full covariance matrix includes extra terms to account for calibration uncertainty and beam uncertainty.

We 'blind' the EB, TB, and BB power spectra throughout our analysis by avoiding estimating them until specific tests are passed. After testing for internal consistency of the data, described in Section 3.3, we unblind the EB and TB power spectra, and after testing a further suite of null tests described in Section 3.7 we unblind the BB power spectra. We do not blind the TT, TE and EE spectra, but do require the same set of consistency and null tests to be passed. We calibrate each power spectrum to *Planck* following Louis et al. (2014), first cross-correlating the D56 PA2 maps with the *Planck* 143 GHz full-mission intensity maps (Planck Collaboration et al. 2016a), and then by correlating the D56 PA1, D5 and D6 maps with the D56 PA2 map.

3.2. *Simulations*

We test the power spectrum pipeline by simulating 840 realizations of the sky. For each one a Gaussian signal is generated on the full sky, drawn from a power spectrum of the sum of the expected signal and foregrounds at 149 GHz. The foreground model used for generating this set of simulations is the same as the data foreground model described in Section 4.1. This neglects the non-Gaussian nature of the foregrounds. The D56, D5, and D6 regions are then cut out and projected onto the flat sky, and a Gaussian noise realization added, drawn from the two-dimensional noise power spectrum estimated from the data by differencing different split maps, and weighted by the data hit count maps. These simulations therefore include appropriate levels of non-white noise, but neglect the spatial variation of the two-dimensional power spectrum. Each set of maps is then processed in the same way as the data.

TABLE 2
Internal consistency tests

Test	Patch	Spectrum	χ^2/dof	P.T.E
Array	D56	TT	0.90	0.69
(PA1-PA2)		EE	0.74	0.91
		TE	0.64	0.98
		TB	0.89	0.69
		EB	1.40	0.03
		BB	0.60	0.99
Array	D56	TT	0.77	0.89
(PA1xPA2-PA2)		EE	0.90	0.68
		TE	1.06	0.35
		TB	0.86	0.76
		EB	1.09	0.31
		BB	0.75	0.92
Season	D56-D5	TT	0.88	0.71
(S2-S1, PA1)		EE	1.08	0.32
		TE	0.83	0.80
		TB	0.89	0.70
		EB	1.07	0.34
		BB	0.68	0.96
	D56-D6	TT	0.93	0.62
		EE	1.09	0.30
		TE	0.98	0.51
		TB	0.94	0.60
		EB	0.96	0.56
		BB	0.99	0.49

Note: Internal tests made to attest the consistency of the power spectra of different subsets of the data

Examining the spectra, we find the dispersion to be consistent with the statistical uncertainty. We construct the data covariance matrix from the simulations, as described further in the Appendix. We also estimate ΛCDM parameters from 100 of these simulations, to test for parameter bias. Since we only have 149 GHz data here, we fix the residual foreground power to the input value, and vary only the six cosmological parameters. Further, since we use only the ACTPol simulated data, we impose a prior on the optical depth and spectral index, with $\tau = 0.08 \pm 0.02$ and $n_s = 0.9655 \pm 0.01$[1]. We find the parameters are recovered with less than 0.2σ bias, where σ corresponds to the uncertainties on cosmological parameters for a single simulation. This also tests the validity of our flat-sky approximation. We also extend the parameter set to include the lensing parameter A_L, which artificially scales the expected lensing potential as in Calabrese et al. (2008a). We estimate this from each of the simulations, and recover $A_L = 1$ to 0.1σ.

3.3. *Data consistency*

To identify possible residual systematic effects, we assess the consistency of the power spectra of subsets of our data, splitting the data by array for D56, by season, and by time-ordered-data split.

Splitting the D56 data by array looks for systematic

[1] Note that after validating the pipeline as described, our final parameter analysis (in Section 5) used an alternative prior for the optical depth and removed the prior on the spectral index.

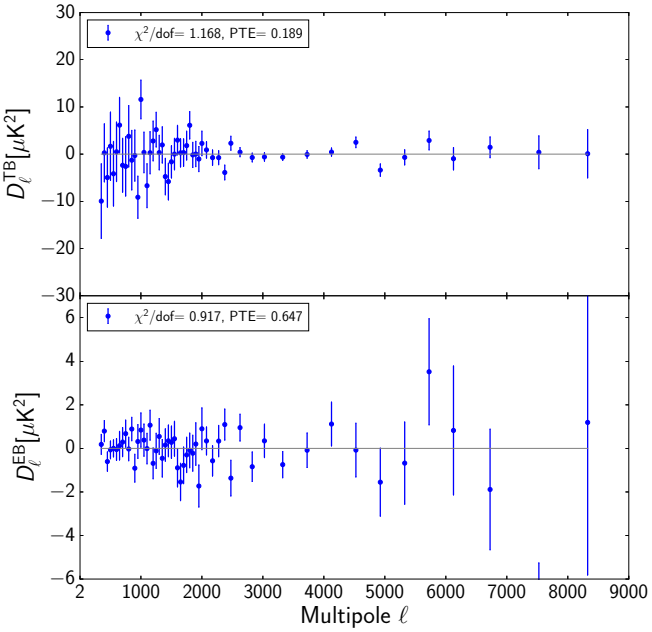

FIG. 6.— The TB (top) and EB (bottom) power spectra, unblinded after internal data consistency checks. The χ^2/dof and probabilities to exceed (PTE) are consistent with the null hypothesis for both spectra.

effects that differ between these two arrays, which could include a number of instrumental effects as the two detector arrays were fabricated and assembled independently. Here we look at the difference between the PA1 and PA2 power spectra, and compute the covariance matrix of this difference using our simulation suite. In fact, it was our first analysis of this null test which indicated a difference between the response of the two arrays, and led to our identification of the beam sidelobes (Figure 4) that differ between PA1 and PA2. Including the beam sidelobe model we find that this test is passed, as indicated in Table 2.

The season test looks for systematic effects in the array or telescope that vary on long time-scales. The sky coverage is not the same between the two seasons, so to perform the season test we cut out just the part of D56 that overlaps with D5 and D6. The results are reported in Table 2 for D56 observed with PA1, and are consistent with null. We also check the difference between the D5 and D6 PA1-S1 spectra and the D56 spectra observed with PA2 in S2, and find no evidence of inconsistency.

After passing this set of consistency tests, we unblind the EB and TB power spectra, shown in Figure 6. The EB and TB power spectra test the polarization angle measurement (e.g., Keating et al. 2013). This can be biased by Galactic foreground emission, but the effect is estimated to be negligible for ACTPol (Abitbol et al. 2016). We vary an overall offset parameter, and find it to be consistent with zero for all our maps, with $\phi = 0.40 \pm 0.26°$ for PA1, and $-0.25 \pm 0.36°$ for PA2. We do not recalibrate the polarization angle, using the original angle estimates as standard. Since these original angle estimates do not yet include a well-characterized systematic uncertainty, we do not estimate cosmological quantities from the EB and TB power spectra.

3.4. *The 149 GHz power spectra*

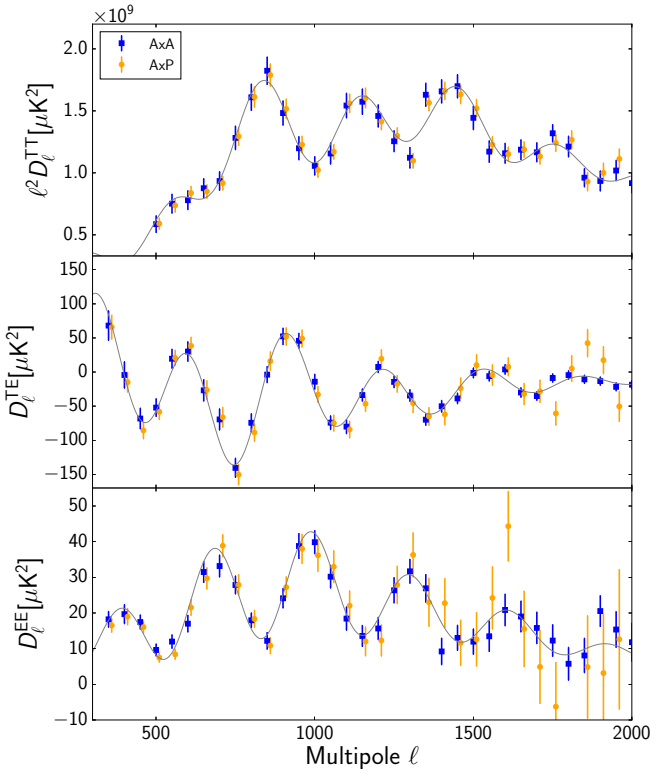

FIG. 7.— Cross-correlation of the D56 PA2 map with the *Planck* 2015 143 GHz temperature and polarization maps. For clarity we shift the ACTxPlanck spectra by $\delta\ell = 10$ compared to the ACTxACT spectra. They are consistent and the relative calibration factor is 0.998 ± 0.007 in temperature, defined such that *Planck* is lower than ACT by that factor.

Given the internal consistency of the spectra, we proceed to calibrate the maps by cross-correlating with the Planck-2015 143 GHz temperature maps. The cross correlation of the D56 PA2 maps with the Planck maps is shown in Figure 7. Here we follow the same method as in Louis et al. (2014). We find the ACT x Planck (AxP) cross-spectra to be consistent with the ACT auto-spectra (AxA): their differences have a reduced χ^2 of 0.68, 1.10, 1.17, with PTE of 0.93, 0.31, 0.22, for TT, TE and EE. No obvious shape dependence or anomalies are detected. The temperature calibration factor is found to be 0.998 ± 0.007. Cross-correlating the D5, D6, D56 PA1 maps with D56 PA2 gives relative calibrations of 1.002 ± 0.012, 0.996 ± 0.01, and 1.009 ± 0.007. We then rescale all the maps to have unit calibration. We do not calibrate our data to *Planck* polarization data, but we test the cross-correlation of the D56 polarization maps with the Planck-2015 143 GHz Q and U maps. The spectra appear consistent, as shown in Figure 7, and the correlation implies an ACTPol polarization efficiency of 0.990 ± 0.025.

The noise levels for these maps are shown in Figure 8, indicating the dominance of non-white atmospheric noise at scales $\ell < 3000$ in temperature. The atmospheric noise is significantly suppressed in polarization, although it dominates the noise power at scales below $\ell \approx 1000$. A powerful technique for suppressing large scale atmospheric noise contamination in polarization is the use of a half-wave plate that modulates the polarization at timescales shorter than most atmospheric fluctu-

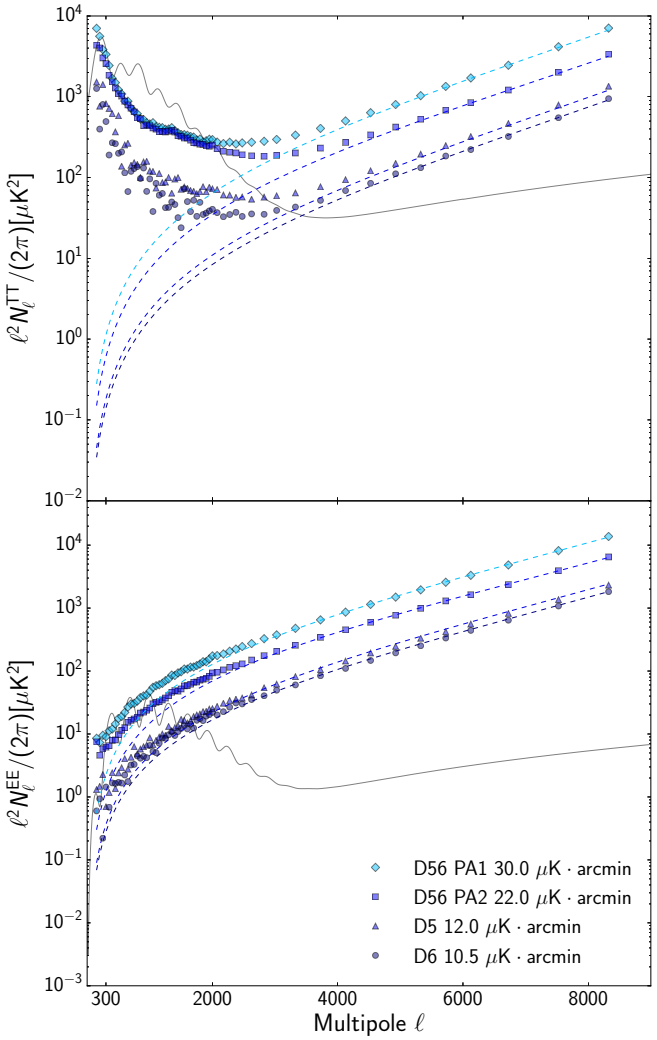

FIG. 8.— Noise levels in the ACTPol two-season maps, with ΛCDM theory spectra included for comparison. In temperature the large-scale noise is dominated by atmospheric contamination. In polarization the contamination is significantly lower, and instrumental noise dominates at $\ell \gtrsim 1000$. The white noise levels given in the legend are shown with dashed lines. These noise curves are from the analysis of roughly half the data that passes quality screening procedures from these two seasons.

ations. The Atacama B-Mode Search telescope (ABS) has shown this results in noise power spectra that are white down to large angular scales (Kusaka et al. 2014). We are currently testing this technique using a subset of ACTPol data taken with a half-wave plate in operation.

The TT, TE, and EE power spectra for the calibrated ACTPol maps in each region are shown in Figure 9, corrected for the transfer function. The temperature and polarization acoustic peak structure is clearly seen in all the maps, with six acoustic peaks measured in polarization. As expected, the D56 maps provide the best estimate of the power at large scales, due to the larger sky area. At smaller scales the deeper D5 and D6 maps contribute more statistical weight. The reference model shown is the best-fitting ΛCDM model with best-fitting foreground contribution, described in section 4.

The optimally combined spectra are shown in Figure 10 for temperature, E-mode polarization, and the TE cross-spectrum, and reported in Table 5. Here, the temperature data have the expected residual foreground contribution that dominates at scales smaller than $\ell \sim 3000$. For comparison, the ACT MBAC temperature data are also shown for the coadded ACT-Equatorial and ACT-South spectra, including 220 GHz data (Das et al. 2014).

3.5. *Real-space correlation*

The *WMAP* team first stacked temperature and polarization data on temperature hot and cold spots to help visualize acoustic patterns in the data (Komatsu et al. 2011). With *Planck* data, the noise of the stacked 2D images was considerably reduced (Planck Collaboration et al. 2016e,g). We now repeat this exercise with the ACTPol data. Although such patterns do emerge in the ACTPol data, there are not as many extrema to stack on and the result is noisier than for *Planck*. To decrease the noise, and provide a direct measure of the TT and TE cross correlation functions $C^{TT}(\theta)$ and $C^{TE}(\theta)$, we instead stack on a much larger set, using randomly chosen temperature field points.

Figure 11 shows the D56 temperature and E-mode polarization maps stacked on a uniformly chosen sample of 'hot' points with $T > 0$, and, with flipped sign, on a 'cold' sample with $T < 0$. For E-polarization, with enough points the result should converge to the ensemble average given the $\{T\}$ constraints, $\langle E(\theta)|\{|T|\}\rangle = C^{TE}(\theta)\langle|T|\rangle/C^{TT}(0)$, where $\langle|T|\rangle$ is the ensemble average of $|T|$ at randomly chosen field points ($\sqrt{2/\pi}\,C^{TT}(0)^{1/2}$). The derivation of this result follows the formalism of constrained realizations of a gaussian field (Hoffman & Ribak 1991). A similar result holds for the mean temperature. Around each stack-point, the T and E fields are randomly rotated, and so should be spherical, as they clearly are. We also show in Figure 12 the one dimensional radial profiles of the stacking of the T, E, B modes on the temperature field points.

The rings in the patterns depend upon the low-pass and high-pass filtering of the maps, but reflect the acoustic patterns in a more direct way than stacking on extrema. To demonstrate that our ACTPol stacks agree with theoretical expectations, in the lower panels of Fig 11 we compare an average of 30 ΛCDM simulations processed in the same way, with ACTPol noise estimated from map differences included. By angle-averaging at each radius we generate direct isotropic correlation function estimates in excellent agreement with the simulations. By varying temperature thresholds, rotation strategies, map selections and data cuts, the stacked maps help show the robustness of the ACTPol data sets. Note that we do not yet stack E on E field points because of the higher noise levels.

3.6. *Galactic foreground estimation*

We estimate the level of thermal dust contamination in the power spectrum using the *Planck* 353 GHz dust maps (Planck Collaboration et al. 2016a). We compute the difference between the power spectrum of the Planck 353 GHz maps and the ACTPol power spectrum at 149 GHz, following a similar method to Louis et al. (2013). The result is shown in Figure 13. The difference between the two power spectra is dominated by CIB fluctuation and Galactic cirrus emissions at 353 GHz. On large and intermediate scales, the contributions from other signals

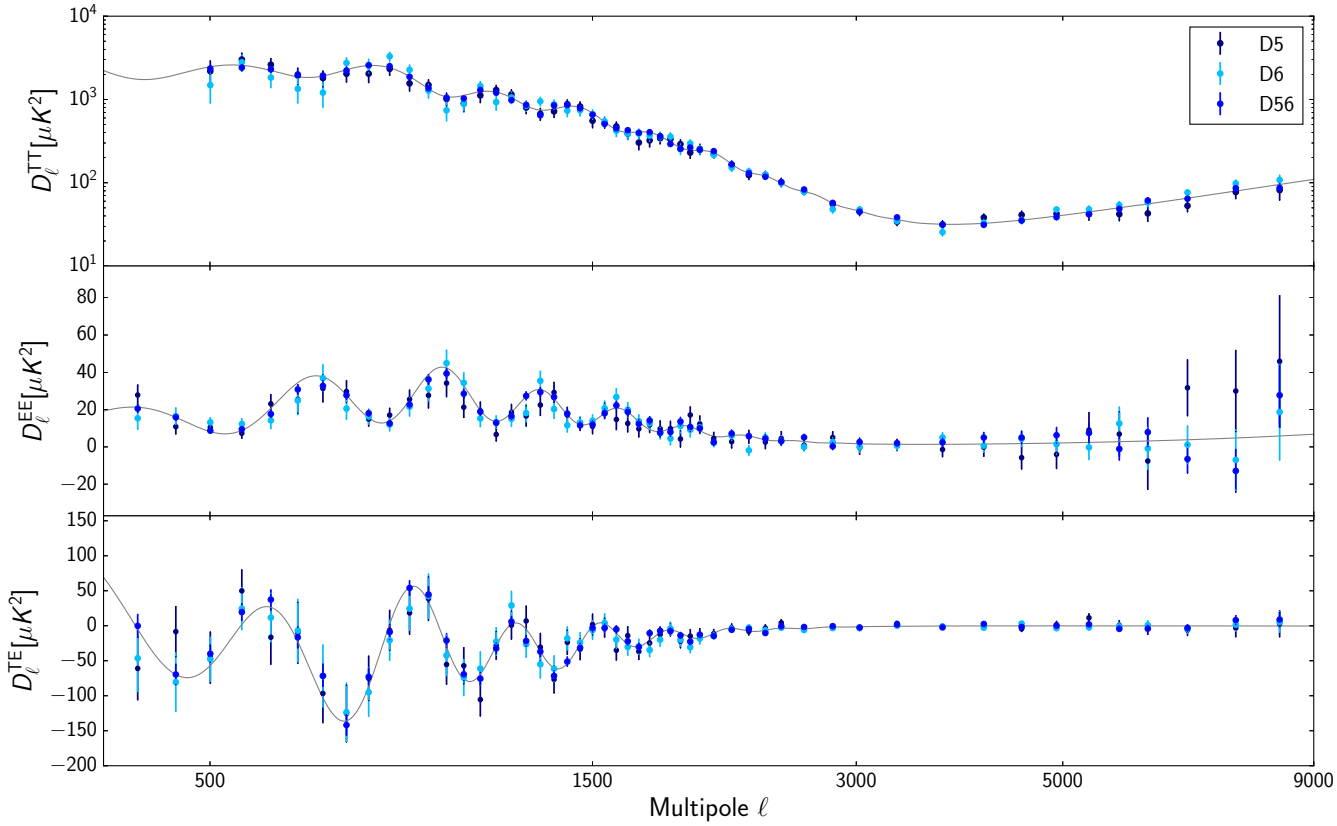

FIG. 9.— The ACTPol power spectra (TT,TE,EE) for individual D56, D5, and D6 patches. For D56 the PA1 and PA2 data have been co-added. The solid lines correspond to the ACTPol best-fit ΛCDM model, including the foreground contribution at 149 GHz.

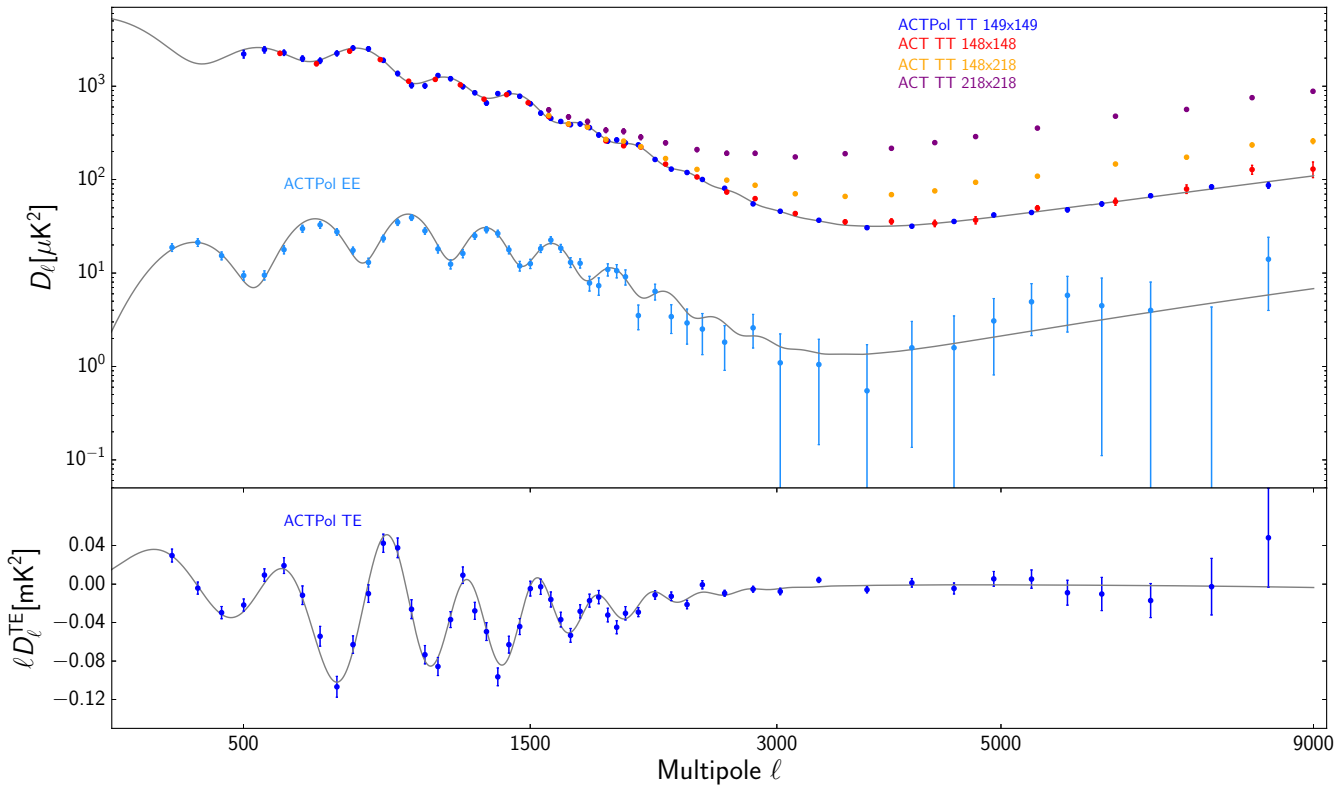

FIG. 10.— Two-season optimally combined 149 GHz power spectra for temperature and E-mode polarization (top), and TE cross-correlation (bottom). The solid lines show the ACTPol best-fit ΛCDM model including the 149 GHz foreground model. The best-fitting foreground model for the 218 GHz data is not shown.

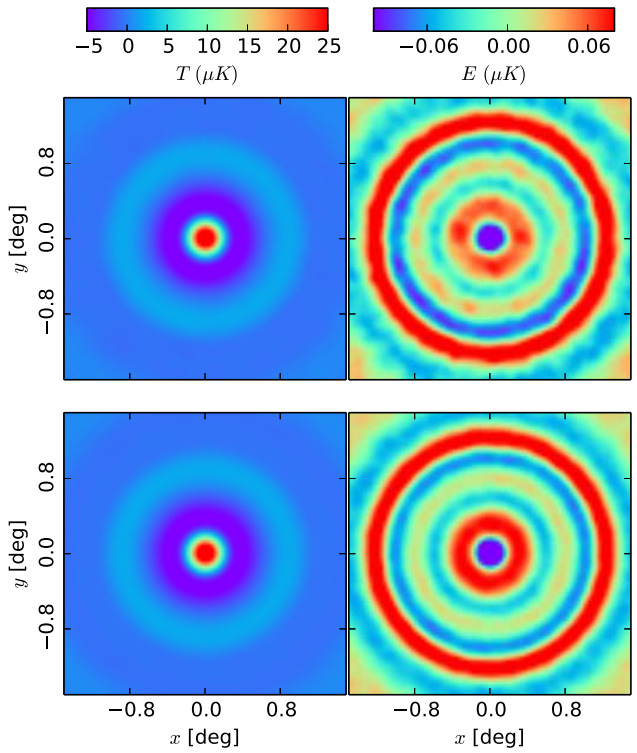

FIG. 11.— The temperature, T, and E-mode polarization maps stacked around randomly selected field points in the temperature map. The sign of the map is reversed when it is stacked around a cold field point with $T < 0$. These provide direct estimates of the TT and TE correlation functions. The top panels show the result from the coadded D56 PA1 and PA2 maps smoothed with a FWHM 5 arcmin Gaussian beam and high-pass filtered with $\ell_{\rm min} = 350$. The bottom panels show the average of 30 simulations generated with Planck-2015 ΛCDM parameters, with noise simulations estimated from the ACTPol data.

are subdominant and can be neglected. The shaded band represents the CIB and dust model from Dunkley et al. (2013), valid for the overlapping ACT-Equatorial region, with the exception of the CIB clustered source template that we have replaced to match the one used in the nominal *Planck* analysis (Planck Collaboration et al. 2014c). We find this model to be a good fit to the 353-149 differenced spectrum, so use the same ACT-Equatorial dust level as a prior in the likelihood. For the angular scales of interest, we find that the polarized dust is not detectable in ACTPol or in Planck 353 GHz. We measured the Planck 353 GHz power spectrum on larger scale and detected a signal. The extrapolation of this signal to smaller scales give negligible signal for all the scales of interest.

3.7. *Null tests*

We make an additional suite of maps to identify further possible systematic contamination. The first set of tests splits the data into two parts. We form the difference map between each part for each split and then compute their cross-spectrum. We test for dependence on the scan pattern by splitting the data for D56 into the two different elevations. We then test the effect of detector performance, making maps from detectors with faster and slower time constants. The threshold is chosen to give roughly equal statistical weight to each subset, splitting at 80 Hz. We test the impact of weather

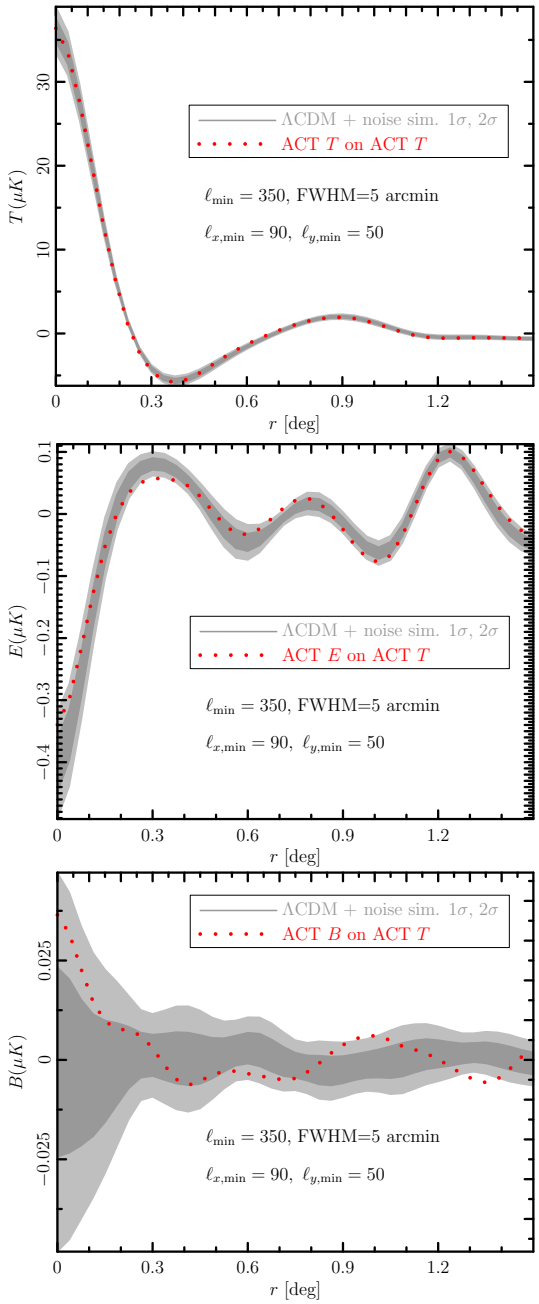

FIG. 12.— One dimensional profiles of the stacked T (top panel) and E (middle panel) maps presented in Fig 11. The bottom panel shows the profile for B stacked around the T field points and is consistent with zero as expected. The oscillations in these profiles depend on the low-pass and high-pass filtering of the maps, but reflect the acoustic patterns. The grey bands represent the 1 and 2 σ uncertainties obtained from ΛCDM simulations.

and atmospheric noise on the data by splitting on precipitable water vapor level (PWV). We choose a threshold of 0.8 mm, again to give equal weight to both halves.

We test the impact of internal telescope pick-up fluctuations by splitting each array into two groups of detectors based on their qualitative behavior. We also run an additional null test for PA2, testing the different detector wafers by splitting the data based on their thermal conductivity to the bath. (For this specific test, the number of detectors in PA1 is too small to pass the internal cuts of the map-maker.) Finally we test the effect of apply-

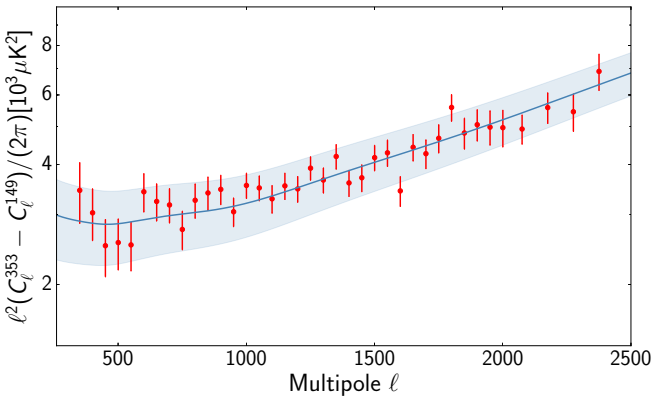

FIG. 13.— Difference between the Planck 353 GHz and ACTPol 149 GHz power spectra in the D56 patch. The band shows the dust+CIB foreground model used for the Das et al. (2014) ACT analysis, with the CIB clustered component template replaced to match that used in the *Planck* analysis. The width of the band reflects the 1σ uncertainties on the parameters of the model. We find good agreement between this model and the data.

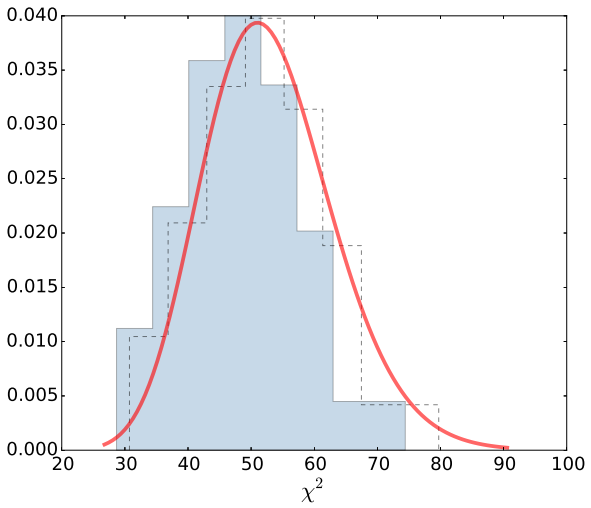

FIG. 14.— Distribution of the χ^2 for the null tests described in Section 3.7. The smooth line represents the expected distribution if the null tests were uncorrelated. The dashed black histogram shows our null test distribution after rescaling the errors by 3%. We interpret this as an indication of overestimation of our errors.

ing a more aggressive moon cut. In all these cases we generate four splits for each map subset, so the power spectrum is estimated from four splits as usual. The χ^2/dof and PTE of all these null tests are reported in Table 3.

We do not find any indication of contamination from any of these systematic effects in the power spectrum. The χ^2 distribution for this set of null tests is shown in Figure 14. The distribution is close to expectation, but we find that the measured and predicted χ^2 distribution fit best if we reduce the error bars by $\approx 3\%$. We interpret this as an indication of overestimation of our errors.

3.8. *Effect of aberration*

The observed power spectra are affected by aberration due to our proper motion with respect to the CMB last scattering surface. We move at a speed of 369 km/s along

TABLE 3
NULL TESTS USING CUSTOM MAPS (PA1, PA2)

Test	Spectrum	PA1 χ^2/dof	PA1 P.T.E	PA2 χ^2/dof	PA2 P.T.E
Scan pattern 1	TT	0.82	0.83	1.00	0.47
v Scan pattern 2:	EE	0.91	0.66	0.72	0.94
(0-1)x(2-3)	TE	0.99	0.49	0.80	0.85
	TB	1.13	0.25	0.86	0.76
	EB	1.15	0.21	0.93	0.61
	BB	0.66	0.97	0.83	0.81
Scan pattern 1	TT	1.13	0.24	1.19	0.17
v Scan pattern 2:	EE	0.67	0.97	1.12	0.25
(0-3)x(1-2)	TE	0.99	0.50	0.83	0.80
	TB	0.85	0.77	0.81	0.84
	EB	0.95	0.58	0.98	0.53
	BB	0.96	0.55	0.75	0.91
Detectors:	TT	0.98	0.51	0.89	0.69
Fast v slow	EE	0.78	0.88	0.72	0.94
	TE	0.94	0.59	0.87	0.74
	TB	1.07	0.34	0.78	0.88
	EB	0.81	0.84	0.68	0.96
	BB	1.02	0.42	1.00	0.48
PWV:	TT	0.99	0.49	1.18	0.18
High v low	EE	0.84	0.78	0.90	0.68
	TE	0.72	0.94	0.71	0.94
	TB	0.75	0.91	0.77	0.89
	EB	0.98	0.52	0.96	0.56
	BB	0.65	0.98	0.94	0.60
Pick up:	TT	1.14	0.22	0.94	0.61
	EE	0.83	0.81	0.64	0.98
	TE	0.87	0.74	0.88	0.72
	TB	0.83	0.80	0.95	0.58
	EB	0.64	0.98	0.95	0.58
	BB	1.00	0.47	0.83	0.81
Moon:	TT	0.82	0.82	1.08	0.32
more aggressive	EE	1.40	0.03	1.18	0.17
cut	TE	1.30	0.07	0.68	0.97
	TB	0.92	0.64	0.91	0.66
	EB	1.01	0.45	0.96	0.55
	BB	0.90	0.67	1.22	0.13
Wafers:	TT			1.02	0.44
Hex1+hex3	EE			1.08	0.33
v hex 2+semis	TE			1.29	0.07
	TB			0.59	0.99
	EB			1.03	0.42
	BB			0.54	0.99

Note: this table reports a series of tests chosen to identify possible systematic contamination in our data. The test are described in Section 3.7

the direction $\boldsymbol{d} = (l, b) = (264°, 48°)$ (e.g. Planck Collaboration et al. (2014b)). This motion induces a kinematic dipole of the form $\cos\theta = (\boldsymbol{d} \cdot \boldsymbol{n})$, where $\boldsymbol{n}$ is the vector position of each pixel. Aberration results in an angle-dependent rescaling of the multipole moments ℓ and its effect on the power spectrum can be approximated as

$$\frac{\Delta C_\ell}{C_\ell} = -\frac{d\ln C_\ell}{d\ln \ell}\beta\langle\cos\theta\rangle \qquad (2)$$

(Jeong et al. 2014), where $\beta = v/c$ and $\langle\cos\theta\rangle = -0.82$ in D56, -0.97 in D5 and -0.65 in D6, where the average is taken over the solid angle of each ACTPol patch. We generate a set of 120 aberrated simulations, compute their power spectra and compare it to the power spectra of non-aberrated maps. The result is presented in Figure

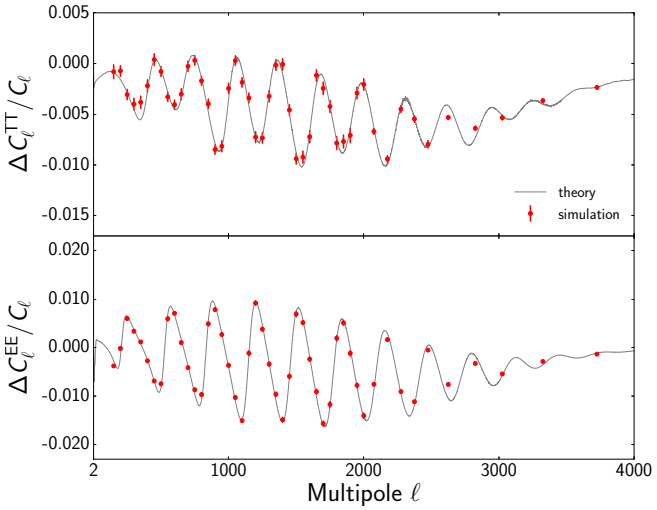

FIG. 15.— Effect of aberration on the TT and EE CMB power spectra due to our proper motion with respect to the CMB. Our aberrated simulations agree with the analytical estimate of the expected effect.

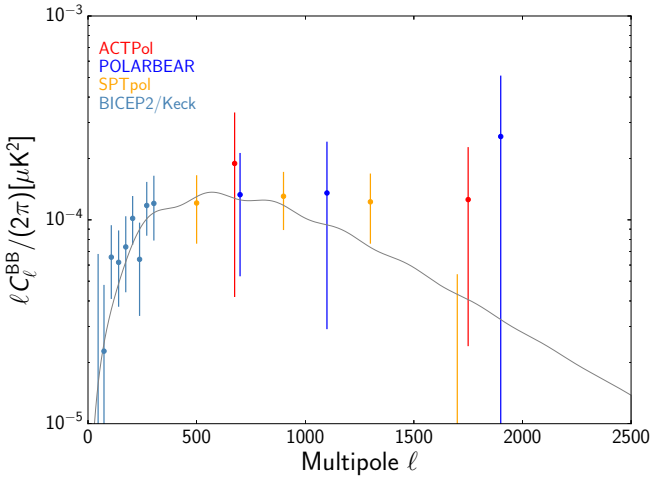

FIG. 16.— Unblinded ACTPol BB power spectra compared to measurements from POLARBEAR (The Polarbear Collaboration: P. A. R. Ade et al. 2014), SPTpol (Keisler et al. 2015) and BICEP2/Keck array (BICEP2 Collaboration et al. 2016). The solid line is the *Planck* best fit ΛCDM model. The ACTPol data are consistent with expectation and deviate from zero at 2σ.

15 together with the analytical estimate. We use this set of simulations to correct our power spectra for the aberration effect, such that $\hat{C}_\ell = C_\ell - \Delta C_\ell$. In earlier releases the effect was negligible compared to our statistical errors and we did not correct for it. Section 5.2 discusses the impact of this correction on cosmological parameters.

3.9. *Unblinded BB spectra*

We unblind the B mode power spectrum at the end of the analysis. The spectrum is shown in Figure 16 along with B mode measurements from The Polarbear Collaboration: P. A. R. Ade et al. (2014), SPTpol (Keisler et al. 2015) and BICEP2/Keck array (BICEP2 Collaboration et al. 2016). We fit for an amplitude in the multipole range $500 < \ell < 2500$, where Galactic and extragalactic contamination is minimal, using the lensed B mode ΛCDM prediction. We find $A = 2.03 \pm 1.01$. This amplitude is consistent with expectation, but the significance of the fit is not high enough to be interpreted as a detection.

4. LIKELIHOOD

We first construct a likelihood function to describe the CMB and foreground emission present in the 149 GHz power spectrum. To improve the estimation of the CMB part, we then add intensity power spectra estimated at both 150 and 220 GHz by the previous ACT receiver, MBAC.

Using these multi-frequency data we estimate the foreground-marginalized CMB power spectrum in TT, TE, EE for ACT, for both the MBAC and ACTPol data. We then combine this likelihood with the data from *WMAP* and *Planck*.

4.1. *Likelihood function for 149 GHz ACTPol data*

Following Dunkley et al. (2013), we approximate the 149 GHz likelihood function $L = p(d|C_\ell^{\rm th})$ as a Gaussian distribution, with covariance described in Sec. 3. We neglect the effects of variation in cosmic variance among theoretical models. The likelihood for the data given some model spectra $C_\ell^{\rm th}$ is given by

$$-2\ln L = (C_b^{\rm th} - C_b)^{\rm T}\mathbf{\Sigma}^{-1}(C_b^{\rm th} - C_b) + \ln\det\mathbf{\Sigma}, \quad (3)$$

where the bandpower theoretical spectra are computed using the bandpower window functions $w_{b\ell}$, $C_b^{\rm th} = w_{b\ell}C_\ell^{\rm th}$, as in Das et al. (2014). We include a calibration parameter y that scales the estimated data power spectra as $C_b \to y^2 C_b$ and the elements of the bandpower covariance matrix as $\mathbf{\Sigma}_{bb} \to y^4\mathbf{\Sigma}_{bb}$. We impose a Gaussian prior on y of 1.00 ± 0.01, using the estimated error from the calibration of ACTPol to *Planck*.

Since we will include data from MBAC data at 150 GHz and 220 GHz, we write the model spectrum as the sum of CMB and foreground terms, following the approach in Dunkley et al. (2013). We use the same intensity foreground model that includes Poisson radio sources, clustered and Poisson infrared sources, kinetic and thermal Sunyaev Zel'dovich effects, and Galactic dust. This model has six free extragalactic foreground parameters: an amplitude for each of tSZ and kSZ spectra, an amplitude for each of the Poisson and clustered infrared spectra, an emissivity index for the infrared sources, and a cross-correlation coefficient between the tSZ and clustered infrared emission. The amplitude for the radio source spectrum is also varied with a prior based on observed source counts, and the spectral index is held fixed. The Galactic dust intensity level has a parameter for each different region (the ACTPol D56 region and the two MBAC ACT regions known as ACT-South and ACT-Equatorial), varied with a prior based on the higher frequency observations. This model all follows Dunkley et al. (2013).

We extend the model to include polarization foregrounds relevant for the ACTPol data, including a single Poisson source term as in Naess et al. (2014) in EE. We allow for an additional Poisson source term in TE that can take both positive and negative values, although this contribution is expected to be negligible.

A similar approach was used for the *Planck* analysis (Planck Collaboration et al. 2016c), which also in-

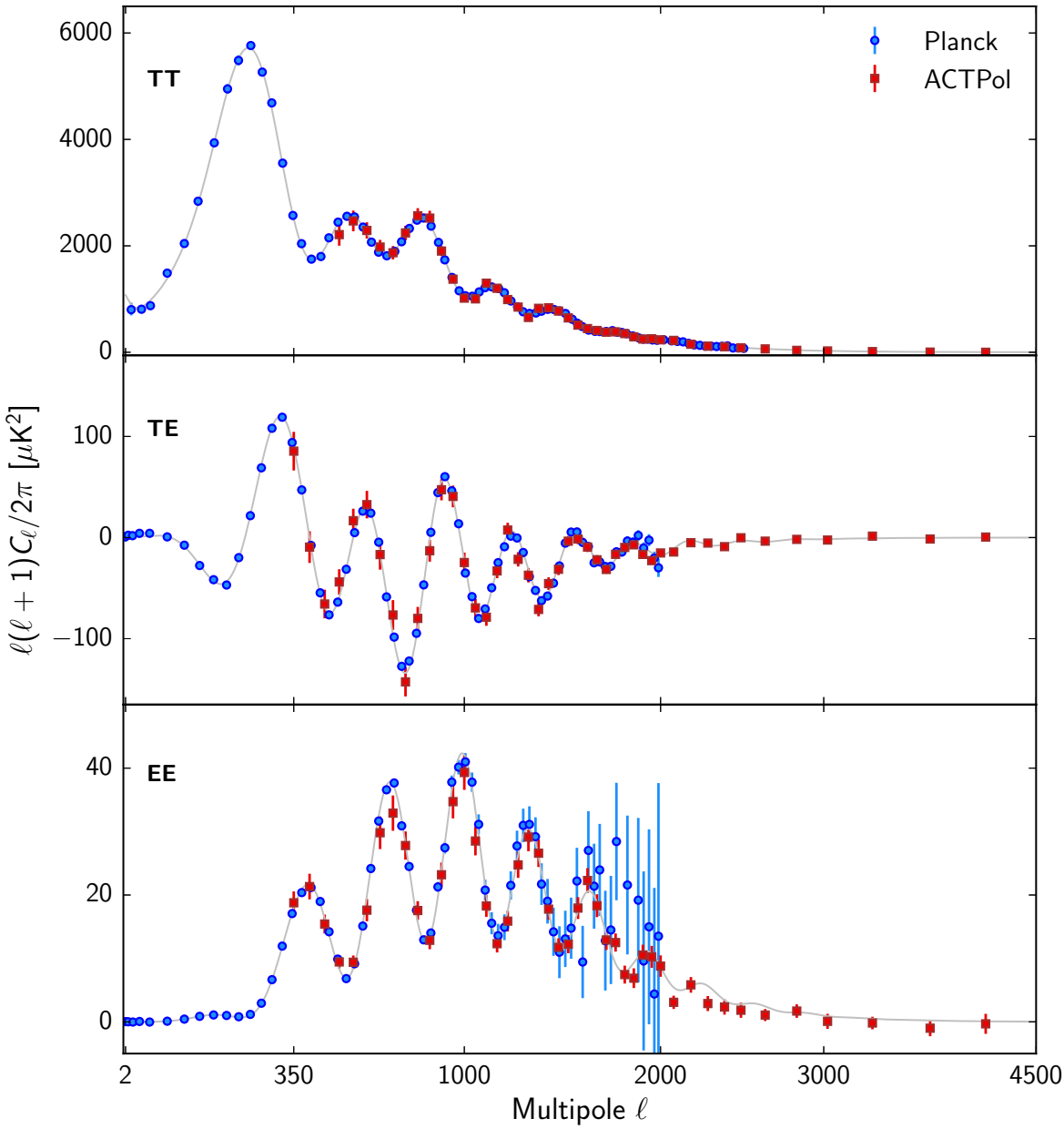

FIG. 17.— Comparison of ACT CMB power spectra (combining MBAC and ACTPol data) with *Planck* power spectra. The uncertainties for ACT are lower than for *Planck* at scales $\ell \gtrsim 1500$ in polarization. The theory model is the *Planck* 2015 TT+lowTEB best-fit (Planck Collaboration et al. 2016c). The small-scale power spectra have also been measured by SPTpol (Crites et al. 2015).

cluded ACT and SPT data, but the foreground model we use for ACT differs in the following few ways. Following Dunkley et al. (2013) we use an alternative cosmic infrared background clustering template that differs at large scales, and an alternative thermal SZ template from Battaglia et al. (2010). This is, however, similar in shape to the Efstathiou & Migliaccio (2012) template used in the *Planck* analaysis. As in Dunkley et al. (2013) we also describe the Poisson source components by using an amplitude and a spectral index for each of the radio and infrared components, rather than a free Poisson amplitude at each frequency and cross-frequency as done for *Planck*.

4.2. *CMB estimation for ACTPol data*

We combine the data from ACTPol and MBAC in the D56 region to estimate simultaneously the CMB bandpower and the foreground parameters, following Dunkley et al. (2013) and Calabrese et al. (2013).

We write the likelihood as

$$-2\ln L = -2\ln L(\text{ACTPol}) - 2\ln L(\text{MBAC}). \quad (4)$$

Here the MBAC data includes both the ACT-S and ACT-E data at 150 and 220 GHz, and the 150-220 GHz cross-correlation.

We use the Gibbs sampling method of Dunkley et al. (2013) to simultaneously estimate the CMB bandpowers and the foreground parameters. We marginalize over the foregrounds to estimate the CMB bandpowers and their covariance matrix. We measure the EE Poisson power to

have $A_p = 1.10 \pm 0.34$, defined in units of μK^2 for D_{3000}. This is evidence for Poisson power in the case where no polarized sources are masked. In the analysis of SPTpol data in Crites et al. (2015), sources with unpolarized flux brighter than 50 mJy are masked at 150 GHz, and an upper limit of $A_p < 0.4$ at 95% CL was found. For ACTPol we find the TE power to be consistent with zero, with $A_{TE} = -0.08 \pm 0.22$ at the same $\ell = 3000$ scale.

The marginalized spectra are shown in Figure 17 and reported in Table 6. Figure 17 also shows how the ACTPol data compare to *Planck* TT, TE and EE data. Due to its larger sky coverage the *Planck* uncertainties are smaller at large scales, but at scales $\ell \gtrsim 1500$ the ACTPol uncertainties in polarization are smaller.

4.3. *Foreground-marginalized ACTPol likelihood*

Following Dunkley et al. (2013), we use the marginalized ACTPol spectrum to construct a new Gaussian likelihood function. The only nuisance parameters in this likelihood are an overall calibration parameter, and a varying polarization efficiency parameter. The likelihood includes data in the angular range $350 < \ell < 4000$, using scales where the distribution of the marginalized spectra is Gaussian to good approximation.

4.4. *Combination with Planck and WMAP*

For some investigations we combine the ACTPol data with *WMAP* and *Planck* data. This is done by adding the log-likelihoods, since there is little overlap in angular range and since the ACTPol survey area represents a small fraction of the sky observed by Planck (Neglecting the covariance between the experiments underestimates the errors by less than 2%.) We use the *Planck* temperature data (Planck Collaboration et al. 2016b) at $2 < \ell < 1000$ as a baseline, and over the full range $2 < \ell < 2500$ for other combined-data tests. This follows the Planck team's recommendation to use only temperature information for high multipoles as the baseline for cosmological analyses. We have confirmed that including the Planck high multipole polarization leads to similar conclusions about data consistency. We label *Planck* temperature at $2 < \ell < 1000$ 'PTTlow'. We use the public CMB-marginalized 'plik-lite' likelihood, constructed using our same marginalization method. The CMB likelihood is then

$$-2\ln L = -2\ln L(\mathrm{ACTPol}) \\ -2\ln L(\mathrm{PlanckTT}_{2<\ell<1000,2500})\,. \quad (5)$$

For TE-only tests we use the *WMAP* likelihood at $\ell < 800$, since it includes TE cross-correlation data (Hinshaw et al. 2013).

Instead of explicitly using the large-scale TE and EE polarization data from *Planck* or *WMAP* we choose to impose a prior on the optical depth of $\tau = 0.06 \pm 0.01$, derived from the *Planck*-HFI polarization measurements (Planck Collaboration et al. 2016h).

5. COSMOLOGICAL PARAMETERS

We use standard MCMC methods to estimate cosmological parameters, using the CosmoMC numerical code (Lewis & Bridle 2002). In the nominal cases we estimate the six ΛCDM parameters: baryon density, $\Omega_b h^2$, cold dark matter density, $\Omega_c h^2$, acoustic peak angle, θ_A (reported in terms of $\theta_{\rm MC}$, an approximation of the acoustic peak angle that is used in CosmoMC) , amplitude, A_s and scale dependence, n_s, of the primordial spectrum, defined at pivot scale $k = 0.05$/Mpc, and optical depth to reionization, τ. All have flat priors apart from the optical depth. We assume $N_{\rm eff} = 3.046$ effective neutrino species, a Helium fraction of $Y_P = 0.24$, a cosmological constant with $w = -1$, and following *Planck* (Planck Collaboration et al. 2016c) we fix the neutrino mass sum to 0.06 eV.

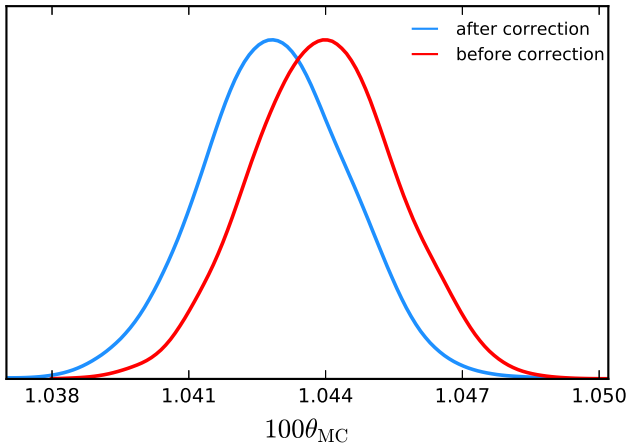

FIG. 18.— Effect of aberration, due to our proper motion with respect to the CMB, on the peak position parameter θ. The corrected power spectrum results in a 0.5σ decrease in the peak position.

We use the aberration-corrected spectra in our analysis, and test the effect on parameters with and without the correction. The ACTPol D56 patch is almost opposite to our direction of motion with respect to the last scattering surface. An observer looking away from his or her direction of motion will measure the sound horizon to have a larger angular size compared to that seen by a comoving observer. As expected, we find a 0.5σ decrease in peak position θ when the correction is applied, as shown in Figure 18. This effect must be accounted for when analyzing small regions of the sky; only over much larger regions does it average out for the two-point function.

5.1. *Goodness of fit of ΛCDM*

We first examine the best-fitting ΛCDM model estimated using only ACTPol data. The model is compared to the data in Figure 19, where we show the residuals in standard deviations as a function of angular scale for TT, TE and EE. This covers both the larger scales where the CMB dominates, and smaller scales where extragalactic foregrounds dominate in intensity. We do not find significant features beyond those expected due to noise. The reduced χ^2 for this fit is 1.04 (for 142 degree of freedom). We find that the ΛCDM model is an acceptable fit to the data.

The parameters estimated from the TT, TE and EE two-point functions are shown in Figure 21. These are consistent with estimates from both *WMAP* and *Planck*, but would need to be combined with large-scale data to give competitive constraints. Despite not measuring the first acoustic peak, ACTPol data are able to constrain the peak position with higher precision than *WMAP* due

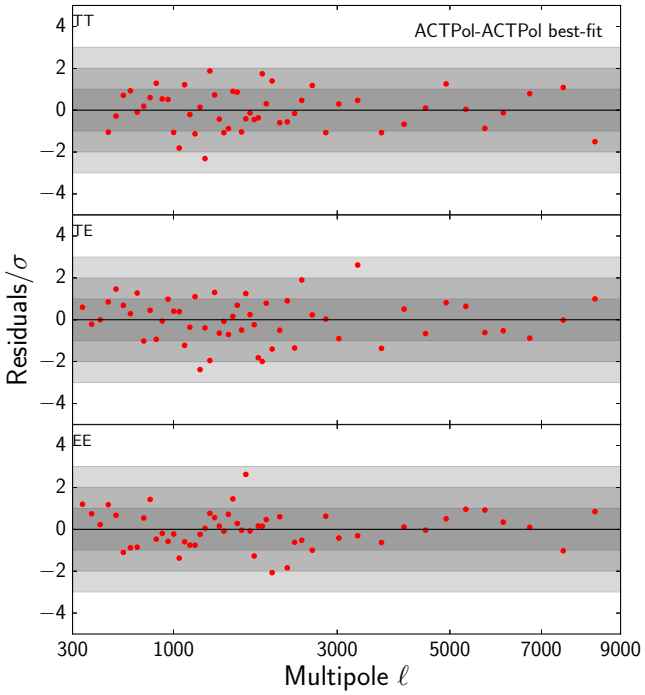

FIG. 19.— The residuals between the ACTPol TT,TE, and EE power spectra and the best-fitting ΛCDM model, in units of σ. The shaded bands show the 1,2 and 3σ levels.

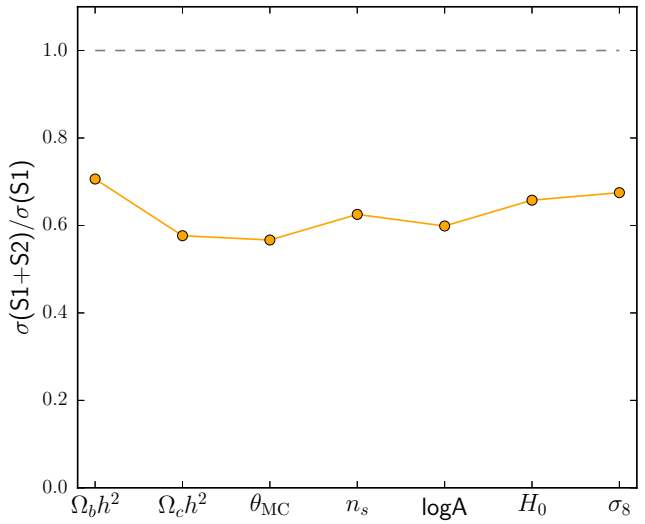

FIG. 20.— The uncertainties in parameters estimated from ACTPol data are reduced from Season-1 to this Season-2 analysis to a factor of 0.6-0.7, gaining from increased observation time and wider sky coverage.

to its measurement over a wide range of angular scales.

5.2. *Comparison to first-season data*

Our second-season D56 data covers approximately twice the sky area observed in D1, D5 and D6 in S1. This reduction in cosmic variance uncertainty, together with the increase in observing time, translates into an improvement in cosmological parameters. In Figure 20, we show the improvement between the Season-1 parameters derived from the Naess et al. (2014) data, analyzed using the same priors as this analysis, compared to the new data used in this paper. Estimates of the means are within 1-σ for all parameters. The individual errors are reduced by a factor of between 1.4 and 1.7, corresponding to a ten-fold reduction in the five-dimensional parameter space volume.

5.3. *Relative contribution of temperature and polarization data*

We then examine the relative contributions of the TT, TE and EE power spectrum in constraining the ΛCDM model, and assess their consistency. We show parameters in Figure 22 and report constraints in Table 4. We find good agreement for parameters derived from TT, TE and EE only spectra, and, for the first time, we find that multiple parameters are better constrained by the TE spectrum than the TT spectrum, using just the data measured by ACTPol.

The ACTPol TE spectrum now provides the tightest internal constraint on the baryon density and the peak position, compared to ACTPol TT and EE, and in turn provides the strongest internal constraint on the Hubble constant. This strength of TE compared to TT was only marginally true for the data from *Planck* (Planck Collaboration et al. 2016c), which had higher noise levels than ACTPol but mapped a larger region of the sky. There, the TE uncertainty on the CDM density was 0.95 the TT uncertainty, but all other ΛCDM parameters were better constrained by TT.

Now, with ACTPol data, the error on the baryon density is 1.8 times smaller with TE than TT, and the peak position error is 1.3 times smaller. The EE spectrum is also starting to make an important contribution; for ACTPol the EE provides the same error on the peak position as the TT.

This is compatible with expectation, as discussed in e.g., Galli et al. (2014), that parameters which are constrained by the position and shape of the acoustic peaks get more weight from polarization data as the noise is further reduced. The peaks and troughs in the temperature power spectrum are less pronounced due to the contribution from the Doppler effect from velocity perturbations that are out of phase with the density perturbations. As a result, the peaks in the TT power spectrum have a lower contrast compared to the peaks in the polarization power spectrum, and the signal to noise on the location of the peaks and their amplitude is higher for polarization data.

In contrast, ACTPol parameters measured using the overall shape of the spectra are currently still better constrained by the temperature power spectrum, in particular the primordial amplitude A_s, because the signal to noise in the damping tail is higher for our two-season ACTPol temperature data.

5.4. *Consistency of TT and TE to ΛCDM extensions*

Given the improved constraining power of TE, we explore whether any extensions of ΛCDM are preferred by TE compared to TT. The TE spectrum offers an independent check of the model, and is not contaminated by emission from extragalactic foregrounds and SZ effects. As such, it is playing an increasingly important role in parameter constraints.

We estimate the lensing parameter A_L, defined in Calabrese et al. 2008b, through its effect on the smearing

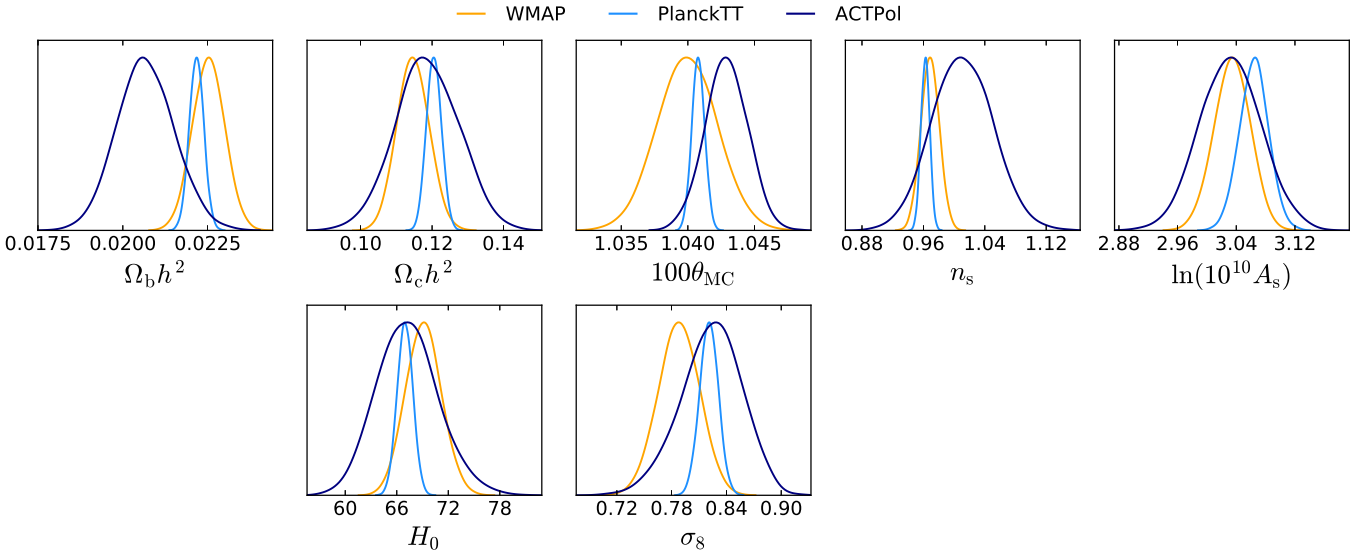

FIG. 21.— Comparison of ΛCDM parameters estimated from *WMAP*, *Planck* and ACTPol data. These likelihoods use 85%, 66%, and 1.4% of the sky respectively.

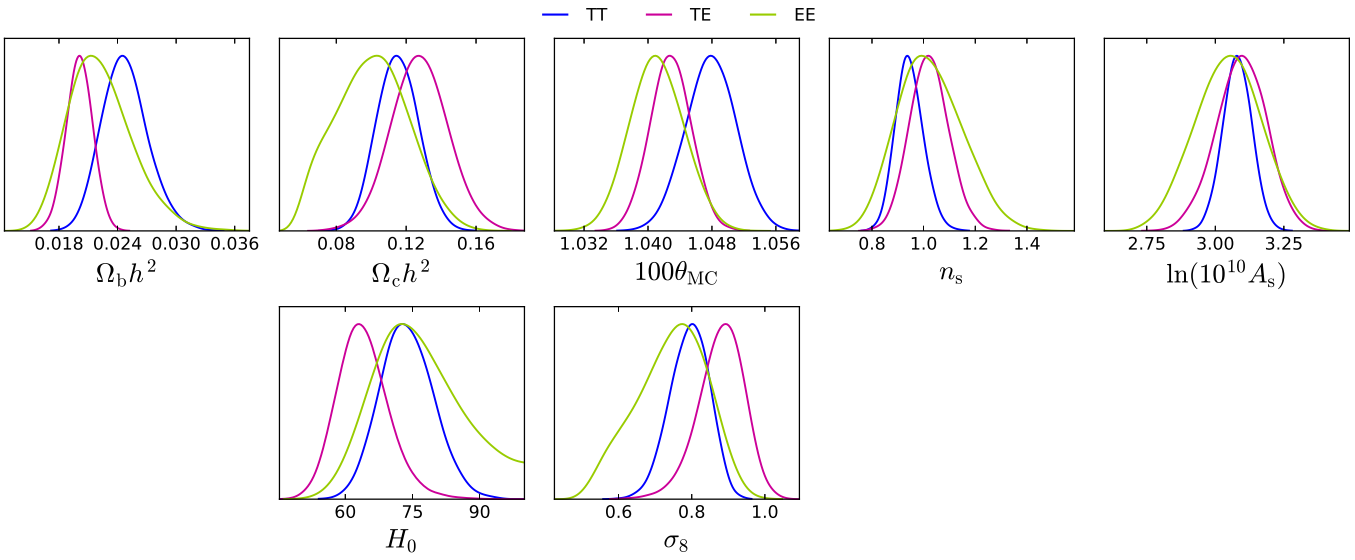

FIG. 22.— ΛCDM parameters as measured by different ACTPol spectra, sampled directly (top) and derived (bottom). The TE spectrum now provides the strongest internal ACTPol constraint on the baryon density, peak position, and Hubble constant.

TABLE 4
COMPARISON OF ΛCDM COSMOLOGICAL PARAMETERS AND 68% CONFIDENCE INTERVALS FOR ACTPOL SPECTRA. A GAUSSIAN PRIOR ON THE OPTICAL DEPTH OF $\tau = 0.06 \pm 0.01$ IS INCLUDED.

	TT	TE	EE	TT+TE+EE
$100\Omega_b h^2$	2.47 ± 0.23	2.01 ± 0.13	2.23 ± 0.34	2.068 ± 0.084
$100\Omega_c h^2$	11.5 ± 1.2	12.8 ± 1.6	10.0 ± 2.0	11.87 ± 0.89
$10^4\theta_{MC}$	104.78 ± 0.32	104.27 ± 0.25	104.12 ± 0.33	104.29 ± 0.16
$ln(10^{10}A_s)$	3.080 ± 0.053	3.096 ± 0.090	3.05 ± 0.12	3.032 ± 0.041
n_s	0.947 ± 0.053	1.022 ± 0.074	1.03 ± 0.12	1.010 ± 0.039
Derived				
σ_8	0.793 ± 0.043	0.880 ± 0.063	0.742 ± 0.094	0.823 ± 0.033
H_0	73.4 ± 5.8	63.4 ± 5.6	76.7 ± 9.4	67.3 ± 3.6

of the CMB acoustic peaks. To reduce degeneracy with other ΛCDM parameters we add the *Planck* temperature and *WMAP* TE data at large scales, where the impact of lensing is minimal, and estimate A_L jointly with the other ΛCDM parameters.

For the TT, TE, and EE data separately, we find

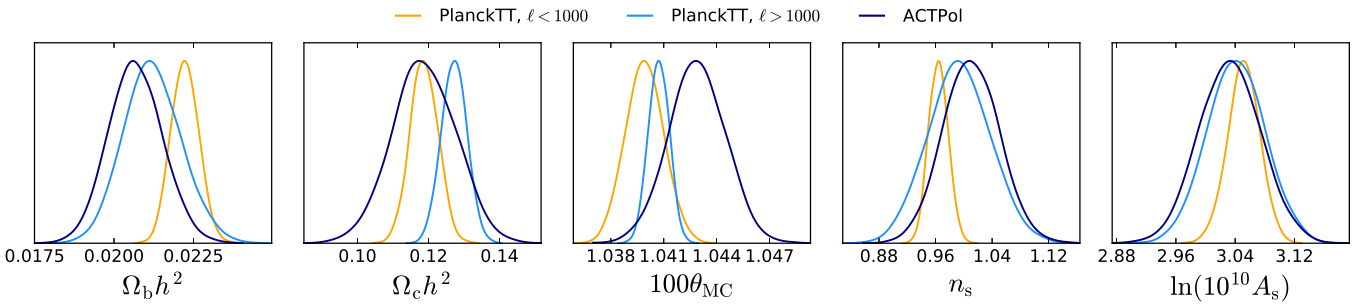

FIG. 23.— Estimates of ΛCDM parameters from ACTPol compared to parameters estimated from large and small multipole ranges of the *Planck* data. Current ACTPol data are consistent with both subsets of *Planck*. All models have a prior on the optical depth.

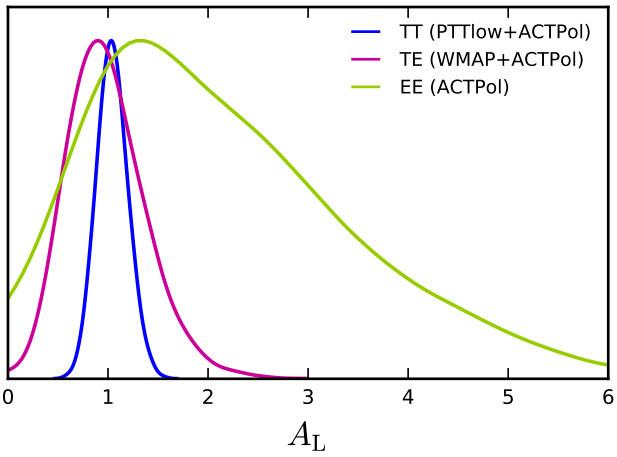

FIG. 24.— Estimates of the lensing parameter A_L using the TT, TE, and EE ACTPol data separately, combined with large-scale data.

marginalized distributions shown in Figure 24, with

$$\begin{aligned} A_L &= 1.04 \pm 0.16 \quad \text{TT (PTTlow + ACTPol)} \\ A_L &= 0.99 \pm 0.40 \quad \text{TE (WMAP + ACTPol)} \\ A_L &= 2.1 \pm 1.3 \quad \text{EE (ACTPol)}\,. \end{aligned} \tag{6}$$

In all three cases we find that A_L is consistent with the standard prediction of $A_L = 1$. The TE power spectrum does not show signs of deviation from the expected lensing signal, and we now measure the lensing in the WMAP+ACT TE power spectrum at 2.5σ significance.

We repeat the same test with the number of relativistic species, and find no evidence of deviation from the nominal $N_{\rm eff} = 3.04$ in the TE or EE spectrum.

5.5. *Comparison to Planck*

Previous analyses of the *Planck* temperature data have shown a 2-3σ difference in some parameters estimated from the small and large angular ranges of the *Planck* dataset (Addison et al. 2016; Planck Collaboration et al. 2016f). We compare parameters derived from our full ACTPol dataset to these two slicings of the *Planck* data. In Figure 23 we show parameters estimated from the ACTPol TT, TE and EE power spectra with parameters obtained from *Planck* temperature data using angular scales greater or smaller than $\ell = 1000$. The ACTPol data presented in this paper are consistent with both sets of parameters estimated from *Planck*. Additional data from the third-season ACTPol observations will shed further light on this issue.

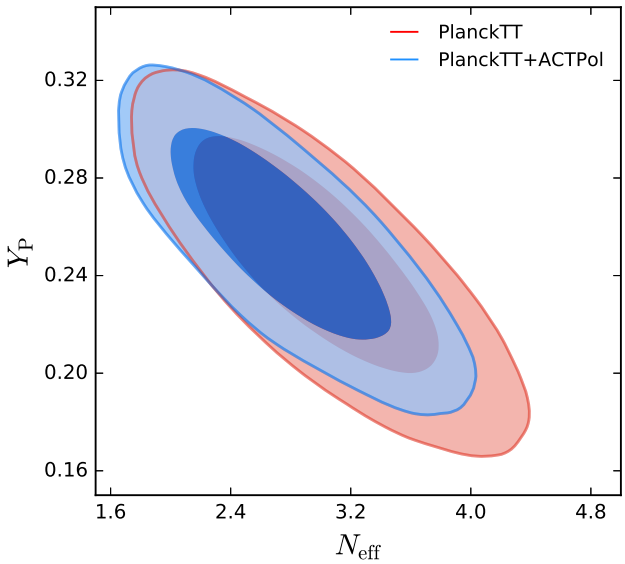

FIG. 25.— Estimates of the number of relativistic species and primordial Helium abundance (68% and 95% CL) from *Planck* temperature data, and *Planck* combined with ACTPol.

5.6. *Damping tail parameters*

Given the consistency of the ACTPol data, both internally and with *Planck*, we add the ACTPol data to the full *Planck* temperature data to better constrain the effective number of relativistic species, and the primordial helium fraction. Figure 25 shows the improvement on the 68% and 95% confidence levels by adding the ACTPol data to the *Planck* temperature data ($2 < \ell < 2500$). We find

$$\begin{aligned} N_{\rm eff} &= 2.74 \pm 0.47 \\ Y_{\rm P} &= 0.255 \pm 0.027 \quad \text{(PlanckTT + ACTPol)} \end{aligned} \tag{7}$$

at 68% confidence level for a joint $N_{\rm eff}$ and Y_P fit. We can compare these values with the ones we obtain from PlanckTT alone: $N_{\rm eff} = 2.99 \pm 0.52$ and $Y_P = 0.246 \pm 0.031$. Additional ACTPol data measuring the damping tail data will further tighten these limits and better test the standard paradigm.

6. CONCLUSIONS

We have presented temperature and polarization power spectra estimated from 548 deg^2 of sky observed at night during the first two seasons of ACTPol observation. We

find good agreement between cosmological parameters estimated from the TT, TE and EE power spectra individually, and the spectra are consistent with the ΛCDM model. The CMB temperature-polarization correlation is now more constraining than the temperature anisotropy for certain parameters; the baryon density and acoustic peak angular scale are now best internally constrained from the TE power spectrum. Adding the new ACTPol polarization data to the *Planck* temperature data improves constraints on extensions to the ΛCDM model that affect the damping tail.

This analysis includes only 12% of the full three-season ACTPol data taken from 2013–15, so future analyses will provide an opportunity to further test the ΛCDM model and more tightly constrain properties including the number of relativistic species, the sum of neutrino masses, and the primordial power spectrum.

This work was supported by the U.S. National Science Foundation through awards AST-1440226, AST-0965625 and AST-0408698 for the ACT project, as well as awards PHY-1214379 and PHY-0855887. Funding was also provided by Princeton University, the University of Pennsylvania, and a Canada Foundation for Innovation (CFI) award to UBC. ACT operates in the Parque Astronómico Atacama in northern Chile under the auspices of the Comisión Nacional de Investigación Científica y Tecnológica de Chile (CONICYT). Computations were performed on the GPC supercomputer at the SciNet HPC Consortium and on the hippo cluster at the University of KwaZulu-Natal. SciNet is funded by the CFI under the auspices of Compute Canada, the Government of Ontario, the Ontario Research Fund – Research Excellence; and the University of Toronto. The development of multichroic detectors and lenses was supported by NASA grants NNX13AE56G and NNX14AB58G. CM acknowledges support from NASA grant NNX12AM32H. JD and SN are supported by ERC grant 259505. EC is supported by a STFC Rutherford Fellowship. TL is supported by ERC grant 267117, by ERC grant 259505, and by the Labex ILP (reference ANR-10-LABX-63) part of the Idex SUPER, and received financial state aid from ANR-11-IDEX-0004-02. HT is supported by grants NASA ATP NNX14AB57G, DOE DE-SC0011114, and NSF AST-1312991. AK has been supported by grant NSF AST-1312380. BS, BK, CM, and EG are funded by NASA Space Technology Research Fellowships. R.D received funding from the CONICYT grants FONDECYT-1141113, PIA Anillo ACT-1417 and BASAL PFB-06 CATA. LM is funded by ALMA-CONICYT grant 31140004. We thank our many colleagues from ABS, ALMA, APEX, and POLARBEAR who have helped us at critical junctures. Colleagues at AstroNorte and RadioSky provide logistical support and keep operations in Chile running smoothly. We also thank the Mishrahi Fund and the Wilkinson Fund for their generous support of the project. We would like to thank the anonymous referee for helpful suggestions that improved the article.

REFERENCES

Abitbol, M. H., Hill, J. C., & Johnson, B. R. 2016, arXiv:1512.06834, MNRAS, 457, 1796

Addison, G. E., Huang, Y., Watts, D. J., Bennett, C. L., Halpern, M., Hinshaw, G., & Weiland, J. L. 2016, arXiv:1511.00055, ApJ, 818, 132

Ade, P. A. R., et al. 2014, arXiv:1312.6646, Physical Review Letters, 113, 021301

Battaglia, N., Bond, J. R., Pfrommer, C., Sievers, J. L., & Sijacki, D. 2010, arXiv:1003.4256, ApJ, 725, 91

BICEP2 Collaboration, et al. 2016, arXiv:1510.09217, Physical Review Letters, 116, 031302

Calabrese, E., Slosar, A., Melchiorri, A., Smoot, G. F., & Zahn, O. 2008a, arXiv:0803.2309, Phys. Rev. D, 77, 123531

—. 2008b, arXiv:0803.2309, Phys. Rev. D, 77, 123531

Calabrese, E., et al. 2013, arXiv:1302.1841, Phys. Rev. D, 87, 103012

Crites, A. T., et al. 2015, arXiv:1411.1042, ApJ, 805, 36

Das, S., Louis, T., Nolta, M. R., & et al. 2014, arXiv:1301.1037, JCAP, 4, 14

De Bernardis, F., et al. 2016, arXiv:1607.02120, in Proc. SPIE, Vol. 9910, Society of Photo-Optical Instrumentation Engineers (SPIE) Conference Series, 991014

Dunkley, J., et al. 2013, arXiv:1301.0776, JCAP, 7, 25

Dünner, R., et al. 2013, arXiv:1208.0050, ApJ, 762, 10

Efstathiou, G. & Migliaccio, M. 2012, arXiv:1106.3208, MNRAS, 3051

Galli, S., et al. 2014, arXiv:1403.5271, Phys. Rev. D, 90, 063504

Hanson, D., et al. 2013, arXiv:1307.5830, Physical Review Letters, 111, 141301

Hildebrandt, H., et al. 2016, arXiv:1606.05338, ArXiv e-prints

Hinshaw, G., Larson, D., Komatsu, E., Spergel, D. N., & et al. 2013, arXiv:1212.5226, Ap J Supp, 208, 19

Hoffman, Y. & Ribak, E. 1991, ApJ, 380, L5

Jeong, D., Chluba, J., Dai, L., Kamionkowski, M., & Wang, X. 2014, arXiv:1309.2285, Phys. Rev. D, 89, 023003

Keating, B. G., Shimon, M., & Yadav, A. P. S. 2013, arXiv:1211.5734, ApJ, 762, L23

Keisler, R., Hoover, S., Harrington, N., Henning, J. W., & et al. 2015, arXiv:1503.02315, ApJ, 807, 151

Komatsu, E., et al. 2011, arXiv:1001.4538, ApJS, 192, 18

Koopman, B., et al. 2016, arXiv:1607.01825, ArXiv e-prints

Kusaka, A., et al. 2014, arXiv:1310.3711, Review of Scientific Instruments, 85, 039901

Lewis, A. & Bridle, S. 2002, Phys. Rev. D, 66, 103511

Louis, T., Næss, S., Das, S., Dunkley, J., & Sherwin, B. 2013, arXiv:1306.6692, MNRAS, 435, 2040

Louis, T., et al. 2014, arXiv:1403.0608, JCAP, 7, 016

Naess, S., Hasselfield, M., McMahon, J., Niemack, M. D., & et al. 2014, arXiv:1405.5524, JCAP, 10, 7

Planck Collaboration, et al. 2014a, arXiv:1303.5076, A&A, 571, A16

—. 2014b, arXiv:1303.5087, A&A, 571, A27

—. 2014c, arXiv:1309.0382, A&A, 571, A30

—. 2016a, arXiv:1502.01582, A&A, 594, A1

—. 2016b, arXiv:1507.02704, A&A, 594, A11

—. 2016c, arXiv:1502.01589, A&A, 594, A13

—. 2016d, arXiv:1502.01591, A&A, 594, A15

—. 2016e, arXiv:1506.07135, A&A, 594, A16

—. 2016f, arXiv:1608.02487, ArXiv e-prints

—. 2016g, arXiv:1605.08633, A&A, 596, A110

—. 2016h, arXiv:1605.02985, ArXiv e-prints

Riess, A. G., et al. 2016, arXiv:1604.01424, ApJ, 826, 56

Sherwin, B. D., et al. 2016, arXiv:1611.09753, ArXiv e-prints

Smith, K. M. 2006, astro-ph/0511629, Phys. Rev. D, 74, 083002

The Polarbear Collaboration: P. A. R. Ade, et al. 2014, arXiv:1403.2369, ApJ, 794, 171

Thornton, R. J., et al. 2016, arXiv:1605.06569, ArXiv e-prints

van Engelen, A., et al. 2015, arXiv:1412.0626, ApJ, 808, 7

APPENDIX

ACTPOL TWO-SEASON POWER SPECTRA

Table 5 shows the combined 149 GHz spectra from D5, D6 and D56, and Table 6 shows the foreground marginalized CMB spectra used for cosmological parameter estimation. The spectra and likelihood presented in this paper are available on LAMBDA: https://lambda.gsfc.nasa.gov/product/act/

TABLE 5
ACTPol Two-season night-time Power Spectra in D56 region, $\mathcal{D}_\ell = \ell(\ell+1)C_\ell/2\pi$ (μK^2).

ℓ	ℓ range	TT		TE		EE		BB		TB		EB	
		$\mathcal{D}_\ell$	$\sigma(\mathcal{D}_\ell)$	$\mathcal{D}_\ell$	$\sigma(\mathcal{D}_\ell)$	$\mathcal{D}_\ell$	$\sigma(\mathcal{D}_\ell)$	$\mathcal{D}_\ell$	$\sigma(\mathcal{D}_\ell)$	$\mathcal{D}_\ell$	$\sigma(\mathcal{D}_\ell)$	$\mathcal{D}_\ell$	$\sigma(\mathcal{D}_\ell)$
350	325 – 375	2452.3	299.5	85.7	19.2	18.8	1.8	0.3	0.3	-10.0	7.9	0.2	0.5
400	375 – 425	1582.8	209.1	-9.5	15.7	21.4	2.0	-0.1	0.3	0.3	6.2	0.8	0.5
450	425 – 475	2005.1	187.9	-65.8	14.1	15.5	1.5	0.1	0.3	-5.0	6.3	-0.6	0.4
500	475 – 525	2219.3	208.4	-44.0	12.6	9.5	1.0	0.0	0.3	1.7	7.3	-0.1	0.4
550	525 – 575	2477.7	194.9	16.7	11.9	9.5	1.1	0.2	0.3	-4.2	6.9	0.0	0.4
600	575 – 625	2298.5	153.1	32.6	13.7	17.7	1.8	0.3	0.3	0.5	6.3	-0.1	0.5
650	625 – 675	1985.6	134.7	-16.9	14.9	29.9	2.6	-0.4	0.4	6.2	5.9	0.1	0.7
700	675 – 725	1878.8	126.0	-76.7	14.7	33.0	2.8	0.1	0.4	-2.4	5.7	0.3	0.7
750	725 – 775	2251.6	135.7	-143.0	14.4	27.9	2.2	-0.1	0.4	-2.6	6.3	0.7	0.6
800	775 – 825	2572.6	144.0	-80.0	11.4	17.7	1.5	0.7	0.4	3.8	6.5	-0.0	0.5
850	825 – 875	2529.5	138.1	-13.1	10.8	13.0	1.4	0.3	0.4	-1.3	6.3	0.9	0.5
900	875 – 925	1910.9	96.0	47.3	10.5	23.3	1.9	-0.1	0.4	-0.3	5.4	-0.9	0.6
950	925 – 975	1381.6	74.2	40.7	10.8	34.9	2.7	0.5	0.5	-9.1	4.5	0.3	0.8
1000	975 – 1025	1025.9	62.2	-24.8	9.9	39.5	2.7	-0.1	0.5	11.6	4.1	0.8	0.8
1050	1025 – 1075	1012.3	59.7	-69.6	9.1	28.7	2.3	0.2	0.5	0.4	4.3	0.4	0.7
1100	1075 – 1125	1307.1	61.0	-78.8	8.5	18.4	1.7	0.2	0.6	-6.7	4.7	-0.0	0.7
1150	1125 – 1175	1211.2	59.3	-33.0	7.2	12.5	1.4	-0.1	0.6	0.3	4.5	1.1	0.7
1200	1175 – 1225	1000.0	51.1	7.4	7.2	16.1	1.6	1.0	0.6	2.8	4.2	-0.7	0.7
1250	1225 – 1275	858.6	38.3	-21.6	7.1	24.9	2.1	0.9	0.6	5.2	3.7	-0.1	0.8
1300	1275 – 1325	663.8	36.3	-37.3	7.1	29.4	2.2	0.1	0.7	0.3	3.7	0.5	0.8
1350	1325 – 1375	835.4	36.4	-71.2	6.8	26.8	2.2	0.8	0.8	2.0	3.8	-0.5	0.9
1400	1375 – 1425	846.7	38.1	-45.6	6.3	18.0	1.7	0.7	0.7	-4.8	3.9	0.2	0.7
1450	1425 – 1475	785.0	36.0	-31.4	5.7	12.0	1.4	-0.3	0.8	-5.8	3.9	0.3	0.7
1500	1475 – 1525	656.0	29.6	-3.6	5.1	12.5	1.4	1.7	0.8	-1.6	3.4	0.3	0.7
1550	1525 – 1575	521.0	24.1	-1.5	5.1	18.2	1.7	0.9	0.9	0.0	3.3	0.4	0.8
1600	1575 – 1625	456.4	20.0	-9.4	4.9	22.6	2.0	-0.5	0.9	3.0	3.1	-0.9	0.9
1650	1625 – 1675	420.8	19.3	-22.0	4.6	18.6	1.8	0.1	0.9	0.3	3.0	-1.5	0.9
1700	1675 – 1725	389.4	18.5	-31.6	4.2	13.3	1.6	0.7	0.9	0.3	2.9	-0.8	0.8
1750	1725 – 1775	396.2	17.4	-16.6	3.9	12.9	1.4	-0.2	0.9	1.8	3.1	-0.3	0.8
1800	1775 – 1825	363.5	16.1	-9.8	3.8	7.8	1.4	0.5	1.0	6.1	2.9	-0.1	0.8
1850	1825 – 1875	303.2	14.3	-7.2	3.7	7.3	1.6	-1.0	1.0	-0.2	2.7	-0.2	0.8
1900	1875 – 1925	261.0	12.5	-16.7	3.7	11.0	1.6	-2.0	1.1	0.0	2.7	0.2	1.0
1950	1925 – 1975	267.2	11.8	-22.9	3.5	10.7	1.7	-1.2	1.1	-1.0	2.7	-1.7	1.0
2000	1975 – 2025	247.9	11.8	-15.3	3.5	9.2	1.7	1.9	1.2	2.3	2.6	0.9	1.0
2075	2025 – 2125	237.5	7.5	-14.3	2.3	3.6	1.0	0.3	0.9	0.9	1.8	0.3	0.6
2175	2125 – 2225	166.1	6.1	-5.1	2.0	6.4	1.2	-1.0	0.9	-0.7	1.6	-0.6	0.7
2275	2225 – 2325	130.4	5.0	-5.5	2.0	3.5	1.2	0.6	1.0	-0.8	1.5	0.3	0.7
2375	2325 – 2425	120.0	4.8	-9.1	1.8	3.0	1.2	0.5	1.1	-3.9	1.6	1.1	0.7
2475	2425 – 2525	101.3	4.2	-0.3	1.7	2.5	1.2	0.7	1.1	2.3	1.5	-1.4	0.8
2625	2525 – 2725	81.4	2.5	-3.6	1.2	1.8	0.9	0.1	0.9	0.4	1.0	1.0	0.6
2825	2725 – 2925	55.4	2.1	-1.9	1.1	2.6	1.0	-1.3	1.0	-0.7	0.9	-0.8	0.7
3025	2925 – 3125	46.2	1.8	-2.5	1.1	1.1	1.1	-0.3	1.1	-0.6	0.9	0.3	0.8
3325	3125 – 3525	36.9	1.2	1.3	0.8	1.1	0.9	1.5	0.9	-0.6	0.7	-0.7	0.6
3725	3525 – 3925	30.7	1.2	-1.5	0.9	0.6	1.2	0.1	1.2	-0.1	0.8	-0.1	0.8
4125	3925 – 4325	31.8	1.3	0.3	1.1	1.6	1.5	1.8	1.4	0.4	0.9	1.1	1.0
4525	4325 – 4725	35.7	1.5	-1.0	1.3	1.6	1.9	2.1	1.9	2.5	1.1	-0.1	1.2
4925	4725 – 5125	41.9	1.8	1.1	1.6	3.1	2.3	-1.6	2.2	-3.4	1.3	-1.6	1.6
5325	5125 – 5525	44.5	2.1	1.0	1.8	4.9	2.8	4.2	2.9	-0.7	1.6	-0.7	1.9
5725	5525 – 5925	47.7	2.4	-1.6	2.3	5.8	3.4	-1.0	3.5	2.9	2.0	3.5	2.4
6125	5925 – 6325	55.0	2.9	-1.7	2.8	4.5	4.4	-0.3	4.5	-1.0	2.4	0.8	3.0
6725	6325 – 7125	67.2	2.8	-2.5	2.6	4.0	4.0	6.9	4.1	1.4	2.2	-1.9	2.8
7525	7125 – 7925	83.8	4.1	-0.4	3.9	-2.2	6.5	3.8	6.4	0.4	3.5	-9.5	4.3
8325	7925 – 8725	86.9	6.4	5.8	6.2	14.1	10.1	19.2	9.6	0.1	5.1	1.2	7.0

TABLE 6
ACTPol Two-season foregound-marginalized Power Spectra in D56 region, $\mathcal{D}_\ell = \ell(\ell+1)C_\ell/2\pi$ (μK^2).

ℓ	ℓ range	TT		TE		EE	
		$\mathcal{D}_\ell$	$\sigma(\mathcal{D}_\ell)$	$\mathcal{D}_\ell$	$\sigma(\mathcal{D}_\ell)$	$\mathcal{D}_\ell$	$\sigma(\mathcal{D}_\ell)$
350	325 – 375	–	–	85.5	19.1	18.8	1.8
400	375 – 425	–	–	-9.4	15.7	21.3	2.0
450	425 – 475	–	–	-65.7	14.2	15.4	1.5
500	475 – 525	2211.2	208.4	-43.9	12.5	9.5	1.0
550	525 – 575	2468.0	194.7	16.7	11.9	9.4	1.1
600	575 – 625	2289.3	153.1	32.6	13.6	17.6	1.8
650	625 – 675	1977.6	134.3	-16.8	14.9	29.8	2.6
700	675 – 725	1870.7	125.7	-76.6	14.7	32.9	2.8
750	725 – 775	2242.3	135.5	-142.7	14.4	27.8	2.2
800	775 – 825	2564.4	143.7	-80.0	11.4	17.6	1.5
850	825 – 875	2521.5	137.8	-13.0	10.8	12.9	1.4
900	875 – 925	1902.2	95.7	47.3	10.5	23.2	1.9
950	925 – 975	1373.1	73.8	40.7	10.8	34.7	2.6
1000	975 – 1025	1017.2	62.0	-24.7	9.8	39.3	2.7
1050	1025 – 1075	1003.7	59.6	-69.6	9.1	28.5	2.3
1100	1075 – 1125	1298.3	60.8	-78.8	8.5	18.3	1.7
1150	1125 – 1175	1202.2	59.0	-33.0	7.2	12.3	1.4
1200	1175 – 1225	990.8	51.1	7.4	7.2	15.9	1.6
1250	1225 – 1275	849.4	38.1	-21.5	7.1	24.8	2.0
1300	1275 – 1325	654.2	36.3	-37.3	7.1	29.1	2.2
1350	1325 – 1375	825.5	36.4	-71.1	6.8	26.6	2.2
1400	1375 – 1425	836.3	38.1	-45.6	6.2	17.8	1.7
1450	1425 – 1475	774.6	36.1	-31.4	5.7	11.7	1.4
1500	1475 – 1525	645.4	29.6	-3.6	5.1	12.3	1.4
1550	1525 – 1575	510.0	24.1	-1.4	5.1	17.9	1.7
1600	1575 – 1625	445.0	20.0	-9.4	4.9	22.3	1.9
1650	1625 – 1675	408.9	19.4	-22.0	4.6	18.3	1.8
1700	1675 – 1725	377.5	18.5	-31.5	4.2	12.9	1.6
1750	1725 – 1775	383.9	17.3	-16.6	3.9	12.5	1.4
1800	1775 – 1825	351.0	16.1	-9.8	3.8	7.5	1.4
1850	1825 – 1875	290.4	14.3	-7.2	3.7	6.9	1.6
1900	1875 – 1925	247.9	12.5	-16.7	3.8	10.5	1.6
1950	1925 – 1975	253.8	11.8	-22.8	3.5	10.3	1.7
2000	1975 – 2025	234.2	11.8	-15.2	3.5	8.8	1.7
2075	2025 – 2125	223.3	7.5	-14.3	2.2	3.1	1.0
2175	2125 – 2225	151.2	6.1	-5.1	2.0	5.8	1.2
2275	2225 – 2325	114.8	5.1	-5.4	2.0	2.9	1.2
2375	2325 – 2425	103.7	4.9	-9.0	1.8	2.3	1.2
2475	2425 – 2525	84.2	4.2	-0.2	1.7	1.8	1.2
2625	2525 – 2725	63.3	2.6	-3.6	1.2	1.1	0.9
2825	2725 – 2925	35.7	2.3	-1.8	1.1	1.7	1.1
3025	2925 – 3125	24.9	2.0	-2.4	1.1	0.1	1.2
3325	3125 – 3525	13.1	1.5	1.4	0.8	-0.2	1.0
3725	3525 – 3925	3.2	1.4	-1.4	0.9	-1.0	1.3
4125	3925 – 4325	0.4	1.5	0.5	1.2	-0.3	1.6

COADDITION OF SPECTRA AND COVARIANCE MATRIX

The power spectra C_ℓ^{XY} ($X, Y = \{T, E, B\}$) presented in this paper are the result of a weighted average of nine data spectra,

$\{d_{56}^{PA1} \times d_{56}^{PA1}, d_{56}^{PA1} \times d_{56}^{PA2}, d_{56}^{PA2} \times d_{56}^{PA2}, d_{5}^{PA1} \times d_{5}^{PA1}, d_{6}^{PA1} \times d_{6}^{PA1}, d_{5}^{PA1} \times d_{56}^{PA1}, d_{5}^{PA1} \times d_{56}^{PA2}, d_{6}^{PA1} \times d_{56}^{PA1}, d_{6}^{PA1} \times d_{56}^{PA2}.\}$

Assuming a Gaussian distribution for these power spectra, their maximum likelihood combination can be easily obtained as

$$C_\ell^{XY,(ML)} = (P^T \mathbf{\Sigma}^{-1} P)^{-1} (P^T \mathbf{\Sigma}^{-1}) \boldsymbol{C}_\ell^{XY}, \tag{B1}$$

where $\boldsymbol{C}_\ell^{XY}$ is a vector encompassing all data spectra, $\mathbf{\Sigma}$ is the covariance matrix of all the different spectra pairs and P is a projection matrix. P^T projects all the individual spectra into a single power spectrum. The covariance matrix of the maximum likelihood spectra is then given by

$$\mathbf{\Sigma}^{(ML)} = (P^T \mathbf{\Sigma}^{-1} P)^{-1}. \tag{B2}$$

We estimate the covariance matrix of all the spectra using 840 Monte Carlo simulations, with

$$\Sigma^{(\alpha A\times\beta B);(\gamma C\times\tau D)}_{\mathrm{WXYZ,\ bb}} = \langle(\hat{C}^{(\alpha A\times\beta B)}_{b,WX} - \langle\hat{C}^{(\alpha A\times\beta B)}_{b,WX}\rangle)(\hat{C}^{(\gamma C\times\tau D)}_{b,YZ} - \langle\hat{C}^{(\gamma C\times\tau D)}_{b,YZ}\rangle)\rangle.$$

Here A,B,C,D stands for detector arrays (PA1 and PA2), α,β,γ,δ stands for season of observation and W,X,Y,Z stands for T, E, B. We use this estimate in the likelihood, and also verify that the dispersion of the simulation is consistent with an analytical estimate:

$$\begin{aligned}\Sigma^{(\alpha A\times\beta B);(\gamma C\times\tau D)}_{\mathrm{WXYZ,\ bb}} = &\frac{1}{\nu_b}\left(S_{b,WY}S_{b,XZ} + S_{b,WZ}S_{b,XY}\right)\\ &+\frac{1}{N_s\nu_b}\left[S_{b,WY}\delta_{\beta\tau}N^{\beta B\times\tau D}_{b,XZ} + S_{b,XZ}\delta_{\alpha\gamma}N^{\alpha A\times\gamma C}_{b,WY} + S_{b,WZ}\delta_{\beta\gamma}N^{\beta B\times\gamma C}_{b,XY} + S_{b,XY}\delta_{\alpha\tau}N^{\alpha A\times\tau D}_{b,WZ}\right]\\ &+\frac{1}{\nu_b}\frac{N_s^2 - N_s(\delta_{\alpha\beta}+\delta_{\gamma\tau}) + N_s\delta_{\alpha\beta}\delta_{\gamma\tau}}{N_s^4 - N_s^3(\delta_{\alpha\beta}+\delta_{\gamma\tau}) + N_s^2\delta_{\alpha\beta}\delta_{\gamma\tau}}\left[\delta_{\alpha\gamma}\delta_{\beta\tau}N^{\alpha A\times\gamma C}_{b,WY}N^{\beta B\times\tau D}_{b,XZ} + \delta_{\beta\gamma}\delta_{\alpha\tau}N^{\alpha A\times\tau D}_{b,WZ}N^{\beta B\times\gamma C}_{b,XY}\right].\end{aligned}$$

Here, S is the signal power spectrum, N represents the noise power spectrum, ν_b is the number of modes in the bin b, and N_s is the number of splits used for computing each cross spectra. The analytic and Monte Carlo estimates are shown in Figure 26. The final covariance matrix is then given by the sum of the signal and noise covariance matrix, the calibration covariance matrix, the beam covariance matrix and a covariance matrix accounting for possible residual leakage estimated using planet map observations

$$\mathbf{\Sigma}^{\mathrm{all}} = \mathbf{\Sigma} + \mathbf{\Sigma}^{\mathrm{cal}} + \mathbf{\Sigma}^{\mathrm{beam}} + \mathbf{\Sigma}^{\mathrm{leakage}}. \tag{B3}$$

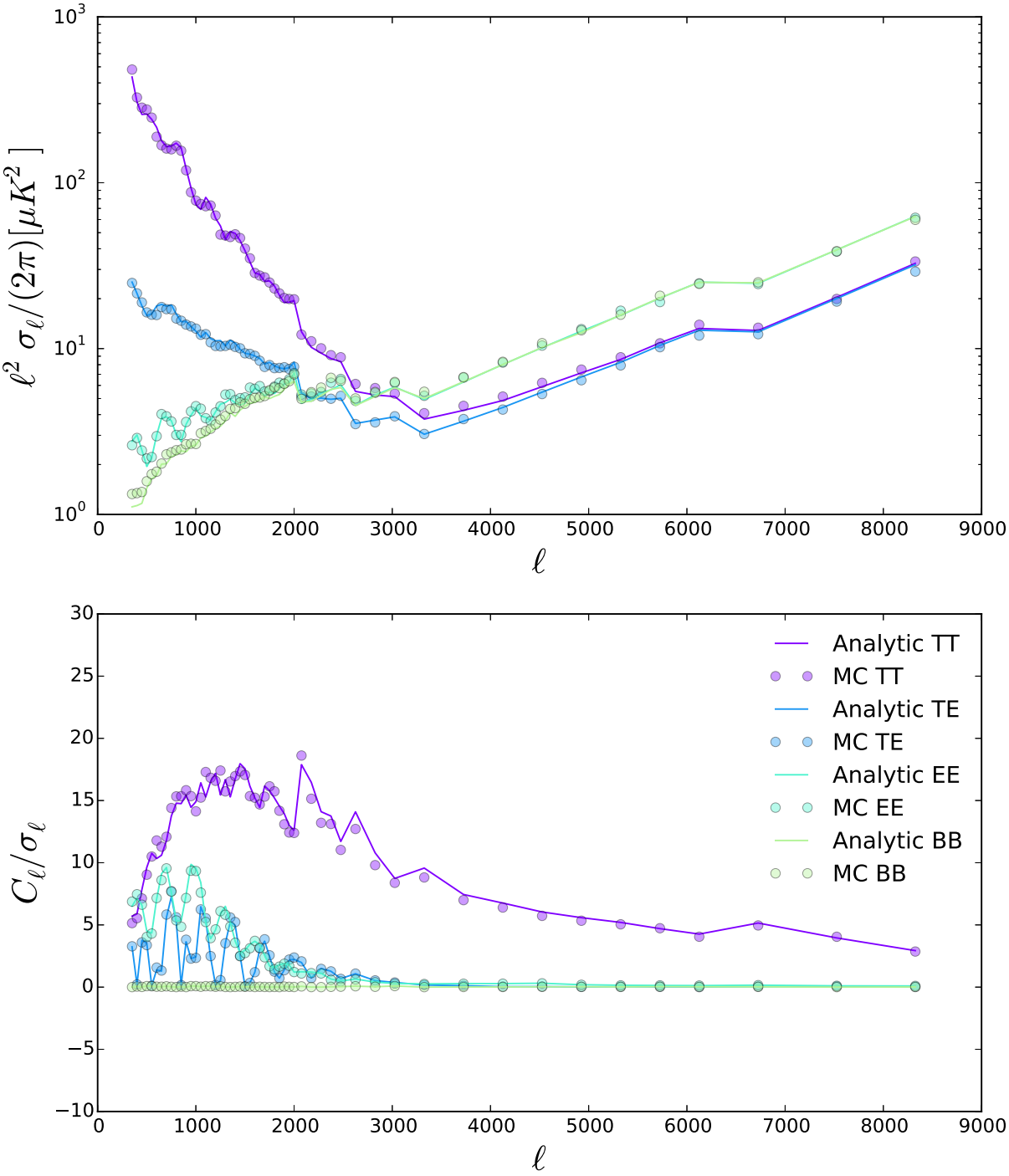

FIG. 26.— Comparison between analytic and Monte Carlo estimates of the errors for D56 PA1. The top panel shows the errors and the bottom panel shows the signal to noise on the TT, EE, TE and BB D56 PA1 spectra.